

of combined optical photometry, spectroscopy, and complete IR data for large samples of very low-mass objects. The first observations of disks around very low-mass stars and brown dwarfs (BD) suggested that they are lower-mass analogs of the typical T Tauri disks. Their disks are flared, show active accretion with strong $H\alpha$ emission, silicate emission from small grains in the disk atmosphere, processed and crystalline silicates, and dust continuum emission down to the far-IR and millimeter wavelengths (Muench et al. 2001; Klein et al. 2003; Mohanty et al. 2004; Jayawardhana et al. 2005; Apai et al. 2005; Scholz et al. 2007; Scholz & Jayawardhana 2008; Harvey et al. 2010, 2012a,b). Many of these observations were biased towards the most luminous disks and stronger accretors. *Spitzer* data suggested that there is an important fraction of harder-to-detect, settled, low-mass, and transitional disks with inner gaps around the very low-mass objects (masses $<0.2 M_{\odot}$ down to the BD regime; Morrow et al. 2008). IR silicate spectroscopy of M-type stars also suggested differences in innermost disk evolution (Kessler-Silacci et al. 2007; Sicilia-Aguilar et al. 2007, 2008; Pascucci et al. 2009). Differences in the disk structure, dead zones, and accretion mechanisms for the lower-mass objects could also change the evolution of the disk and the formation of planets around very low-mass stars (Hartmann et al. 2006).

More recent observations suggest that the stellar mass is not the only parameter that controls the disk structure and subsequent evolution. Studies of stars in sparse clusters vs. more populous star-forming regions point to differences in the disk fraction vs. age trend. Sparse clusters would have relatively lower disk fractions at an early age, but these disks may survive for longer timescales compared to more massive regions (Fang et al. 2013a). The *Herschel* Space Telescope has traced the typical sizes and structures where young stars are formed (Arzoumanian et al. 2011; Hacar et al. 2013), revealing the details of star-forming filaments. Surprisingly, some sparse associations, instead of being quiet low-mass star-forming regions, appear to be very crowded, active, and interactive already at a very early stage (Sicilia-Aguilar et al. 2013). The cluster dynamics, interactions, and angular momentum in the collapsing cloud could also affect the initial mass function (IMF) and the disk properties and subsequent evolution (Hsu et al. 2012, 2013; Becker et al. 2013; Dullemond et al. 2006).

With this work we want to address disk evolution and its dependency on stellar mass/spectral type and environment by studying the low-mass members in the Tr 37 cluster. Tr 37 is located at 870 pc distance (Contreras et al. 2002) and part of the Cep OB2 complex (Platais et al. 1998; Patel et al. 1995, Patel). The cluster is a key region for disk evolutionary studies due to its intermediate age (~ 4 Myr; Sicilia-Aguilar et al. 2005) compared to the typical disk lifetimes (3–10 Myr; Sicilia-Aguilar et al. 2006a; Hernández et al. 2007; Fedele et al. 2010). Multiwavelength studies (Sicilia-Aguilar et al. 2004, 2005, 2006a,b; from now on SA04, SA05, SA06a, and SA06b) have targeted the solar-type population in the region, finding evidence of substantial disk evolution and dust processing (SA06a; Sicilia-Aguilar et al. 2007, 2011b, from now on SA11). Detailed $H\alpha$ photometry surveys (Barentsen et al. 2011) revealed an extended population of accreting stars, some of which could be younger than the main cluster (SA05, Getman et al. 2012).

The disk structure for the solar-type population has been already extensively discussed in SA06a and SA11. Using a combination of optical (photometry and spectroscopy), *Spitzer* (IRAC, MIPS, and IRS), and millimeter-wave (IRAM) data, together with simple radiative transfer models (RADMC;

Dullemond & Dominik 2004), we constrained disk parameters and deviations from typical, uniform, flared disks. Here we present a detailed multiwavelength study of the low-mass population in Tr 37. By using optical spectroscopy, we were able to classify more than 200 objects among cluster members and probable members, including 78 newly identified members, most of them M-type stars. Combining this information with our previous optical photometry and *Spitzer* IRAC and MIPS data, we analyze the disk characteristics of the objects and put them in context comparing them to our previous study of the solar-type stars. All observations are presented in Sect. 2. In Sect. 3 we examine the membership of the candidates and derive their fundamental stellar properties. In Sect. 4 we explore the implications of the newly discovered objects for disk dispersal and evolution. Finally, Sect. 5 summarizes our results.

2. Observations and data reduction

2.1. Optical and IR data and candidate selection for spectroscopy

This study aimed to complete the previous work of SA05/SA06a/SA11 on the disks around solar-type stars in the Tr 37 cluster, which was approximately complete for stars with spectral types K4–M2, by addressing the M-type population in the cloud. Optical photometry and spectroscopy are required to confirm the cluster membership, to obtain spectral types, to detect accretion, and to estimate extinction, age, and stellar mass. The starting point of the target selection was the deep optical photometry obtained at Calar Alto Observatory with the LAICA camera on the 3.5 m telescope, consisting of deep observations with the standard *UVRI* Johnsons filters (see Sicilia-Aguilar et al. 2010 for a detailed description of the observations and data reduction). The data had a large dynamical range, being complete in the range $U \sim 15\text{--}21$, $V \sim 13\text{--}21$, $R_J \sim 12\text{--}21$, and $I_J \sim 11\text{--}20$ mag. The low-mass candidates relevant for our survey were in general too faint to be detected with the U band filter. The requirement for the objects to be preferably candidate M-type members resulted in a selection of objects with $R_J = 17\text{--}20.5$ mag, considering that the extinction over Tr 37 is moderate and relatively uniform ($A_V = 1.56 \pm 0.55$ mag). Examining the 2MASS (Cutri et al. 2003) counterparts of our optical targets allowed to refine the selection of objects consistent with diskless late-type stars and the locus of classical T Tauri stars (CTTS) in the $J - H$ vs. $H - K$ diagram (Bessell & Brett 1988; Meyer et al. 1997), although for M-type stars with evolved disks, the excesses in H and K bands are usually very small or negligible. The 2MASS coordinates were also used for the later spectroscopy, given the strong requirements of multiobject spectrographs.

To complete the spectral energy distributions (SEDs) of the candidates, we re-reduced the *Spitzer* IRAC and MIPS observations (from both our previous datasets in SA06a, and *Spitzer* archival data), following the method described in SA11. These new photometry is not significantly different from that of SA06a, although the use of a more recent pipeline with improved flat fielding, and smaller apertures result in more accurate magnitudes for the in-cloud sources and a better detection of very faint objects in the MIPS $24 \mu\text{m}$ maps. To ensure that contamination by cloud emission or ghosts remains minimal, we visually inspected all the candidates. In particular, detailed inspection of the $24 \mu\text{m}$ data was necessary to remove objects suffering from nebular emission.

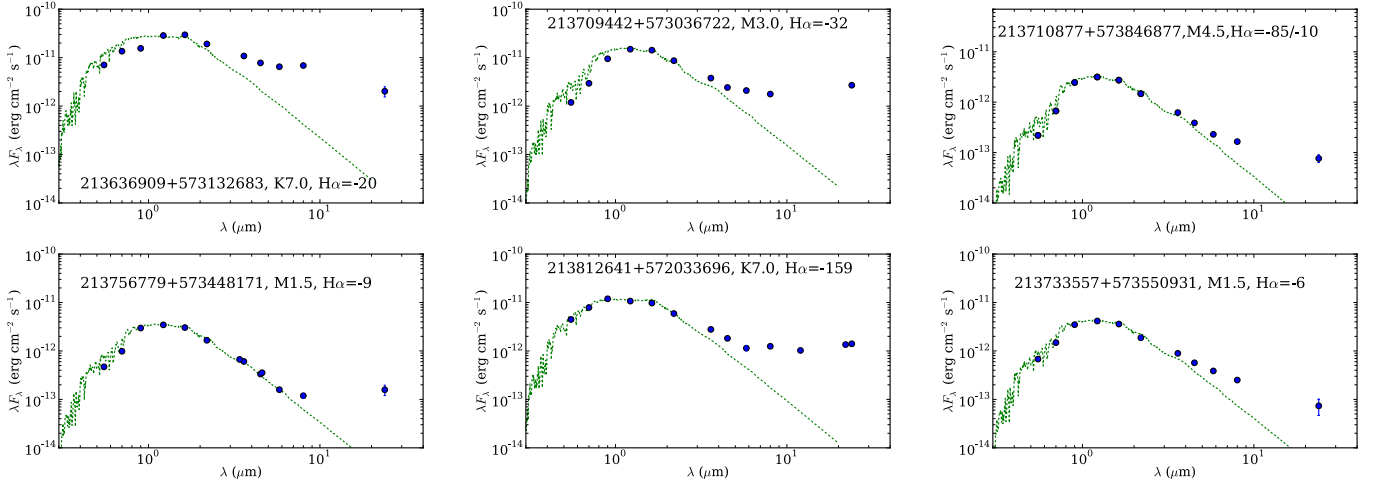


Fig. 1. Examples of SEDs of some of the members with IR excess. For comparison, the photosphere of a star with the same spectral type from the MARCS models (Gustafsson et al. 2008) is displayed. All datapoints have been extinction-corrected according to their individual values of A_V and assuming a standard extinction law (see Table A.1). Information about the $H\alpha$ EW (in Å) is also displayed. The rest of SEDs of objects with IR excesses are displayed in the online material.

For the spectroscopic followup, we selected the sources with ages under 100 Myr that were consistent with solar- and M-type stars at 870 pc distance according to the V vs. $V-I$ and $V-R$ diagrams and the Siess et al. (2000) isochrones. This produced a list of about 400 targets, of which approximately 100 had IR excesses consistent with circumstellar disks and that lacked spectroscopic characterization. We assigned priority to allocating the fibers and slits to objects with IR excess, followed by those with isochrone ages <10 Myr, and finally those between 10–100 Myr. All the observed targets are listed in Table A.1, together with the relevant information about $H\alpha$, Li I emission, presence of disks, spectral type, extinction, and membership (see Sect. 3 for details). A few remaining fibers were assigned to previously known objects, or to objects with strong IR excesses but lacking optical data. This study is thus biased towards objects with disks, so we cannot estimate the disk fraction. The main advantage is that we covered more than 90% of the candidate M-type stars with IR excesses, obtaining a superb dataset to explore the various disk structures. The photometry data (optical, 2MASS, and *Spitzer*) are listed only for the members and probable members in Tables A.2 and A.3.

For completeness, after the survey we also checked the WISE database for counterparts to our objects. The *Spitzer* data are preferred because the larger WISE beam often suffers from strong contamination due to cloud emission, resulting in overestimated fluxes, especially in bands 3 and 4. Nevertheless, band 3 ($12\ \mu\text{m}$), together with IRAC $8\ \mu\text{m}$, offers valuable information regarding the silicate emission. Whenever there was a good agreement between IRAC and WISE bands 1 and 2, MIPS $24\ \mu\text{m}$ and WISE band 4 ($22\ \mu\text{m}$), we assume there is no significant contamination and thus use the $12\ \mu\text{m}$ WISE data. The WISE fluxes were obtained applying the Wright et al. (2010) color corrections depending on the *Spitzer* SED shape. The WISE data used in this project are also listed in Table A.4.

The spectroscopic properties of the observed objects and membership criteria are described in Sect. 3. Thanks to the strong candidate selection criteria, the efficiency of the survey was very high, with about 90% of candidates with isochronal ages younger than 10 Myr and IR excesses being confirmed as cluster members. The success rate fell down to ~ 5 –20% among

the objects without excess. A number of objects with very low signal-to-noise ratio (S/N) could not be ruled out nor confirmed as members (see Table A.1). A few examples of SEDs of members with IR excesses are shown in Fig. 1. The SEDs of all members and probable members with IR excesses are displayed in Figs. B.1–B.6, and the SEDs classification criteria are discussed in Sect. 4.1.

2.2. SCORPIO multislit/6 m Russian SAO RAS Telescope

One observational campaign took place with the Spectral Camera with Optical Reducer for Photometric and Interferometric Observations (SCORPIO) multislit spectrograph (Afanasiev & Moiseev 2005) at the 6 m telescope of the Special Astrophysical Observatory of the Russian Academy of Sciences, in the Northern Caucasus. The observations were obtained during 2008 October 4–6. SCORPIO is a multislit spectrograph with 16 movable long slits (each of $18''$) that can be placed over a $2.9 \times 5.9\ \text{arcmin}^2$ field. We observed 3 configurations, with slits allocated to cover between 12 and 16 candidate objects. We used the grism VPHG1200r, with a spectral coverage 5700 – $7500\ \text{\AA}$ and a $5\ \text{\AA}/\text{pix}$ resolution. Due to the poor weather conditions, we had to reduce the exposure time to 3×15 – 10 min per field.

The observations were reduced following standard IRAF¹ procedures within the *specred* package, in particular, routines within the *twodspec.apextract* package. The spectra were bias-corrected, flat fielded, and extracted. The wavelength calibration was performed with a Ne lamp, observed with the same slit configuration as the datasets. The sky subtraction was done by using the sky spectra adjacent to the star in the slit. A total of 18 new member candidates were identified among the observed objects. The main limitation of these observations was the poor S/N of the data, due to the poor weather conditions, that did not allow us to clearly detect the Li I absorption in most of the candidates. We therefore re-observed many of these objects in our subsequent spectroscopic program with the MMT. The advantage of using

¹ IRAF is distributed by the National Optical Astronomy Observatories, which are operated by the Association of Universities for Research in Astronomy, Inc., under cooperative agreement with the National Science Foundation.

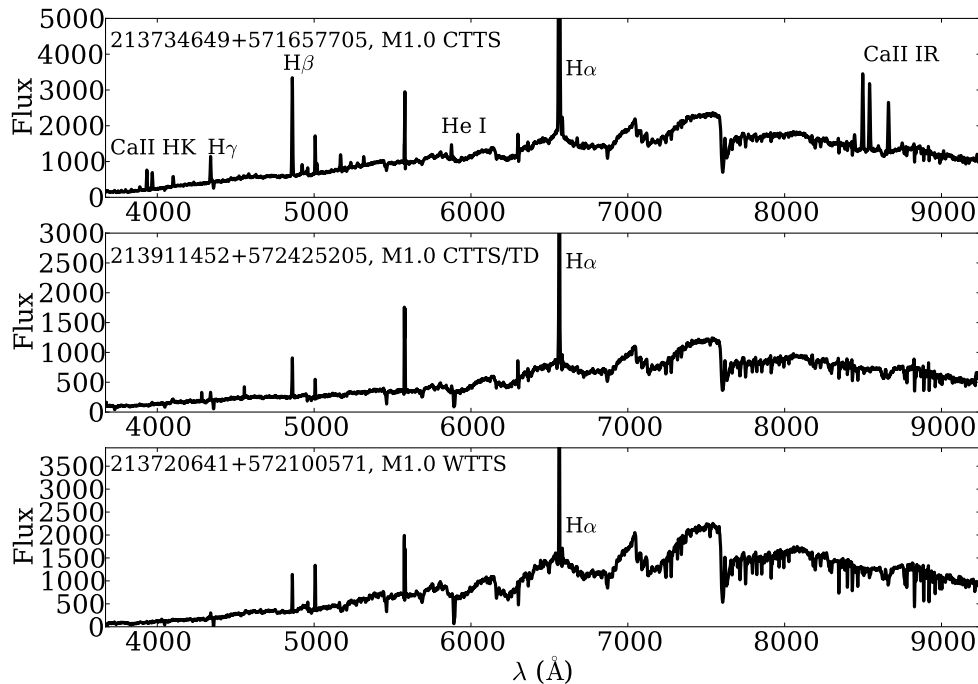


Fig. 2. Some examples of spectra taken with the MMT/Hectospec. The $H\alpha$ features are cut to reveal more details of the whole spectra. Note that the spectra still show some telluric lines in emission (mostly at 5577 and 5004 Å). The flux is in arbitrary instrumental units.

SCORPIO is that the long slit data allow unambiguous subtraction of the nebular emission around the sources.

2.3. Hectospec/MMT spectroscopy

The candidate objects were observed during two campaigns with the multifiber spectrograph Hectospec on the 6.5 m MMT telescope in Mount Hopkins, AZ. The first set of observations were taken on 2009 July 14 and 19, and the second one on 2010 May 17 and 19. The weather conditions were fair during both campaigns. Hectospec is a multifiber spectrograph with 300 fibers that can be allocated to individual objects or sky over a 1 degree field of view. We took a total of 3 configurations, each one including between 180 and 220 candidate objects, plus numerous sky positions. We used the 270 gpm grating, with a spectral coverage from ~ 3650 – 9200 Å and a typical resolution of 5 Å. This is the same setup we used for the observations of the solar-type stars (SA05). For each field, we took 3×30 min exposures, followed by sky observations obtained by shifting the whole configuration by $5''$ and exposing 3×10 min. These sky observations are particularly useful to attain a good sky subtraction in the cases of faint targets or objects in regions with complicated background, since they provided the sky spectrum in a region very close to the objects, and obtained with the same fiber.

The bias, flat fielding, and wavelength calibration were done with standard IRAF tasks within the *dofibers* package. For the wavelength calibration, we used a HeNeAr calibration lamp. Due to the offsets between the even- and odd-numbered fibers, the wavelength calibration was done separately for the even and odd fibers. The one-dimensional spectra were extracted and combined before the sky subtraction. The sky subtraction can be a problem in regions like Tr 37, where substantial, spatially-variable emission from the H II region can affect the $H\alpha$ line, one of our main membership diagnostics. For each night, we classified all the sky spectra in “bright”, “medium”, and “faint”, according to the intensities of the nebular emission

lines (especially, $H\alpha$, [N II], and [O I]), combining the three sets to create bright, medium, and faint sky templates. Each template resulted from a minimum of 20 spectra. The three templates were subtracted from all the objects, and we then examined the success of each sky subtraction by checking the night sky and nebular emission lines. We then selected the best-subtracted spectrum. For about a fourth of the objects, none of the three sky subtractions provided a good result (either by excess or by defect). In those cases, we used the wavelength-calibrated individual sky spectra taken in the proximity of the star, which improved the subtraction of the nebular and night sky lines, although the difference in exposure time resulted in a higher noise than in the cases where the sky template spectra were applied. Some examples of spectra are shown in Fig. 2.

2.4. CAFOS/2.2 m Calar Alto narrow band imaging

Since our previous spectroscopic surveys had revealed substantial forbidden line emission in the Tr 37 globule, we also performed a narrow band imaging in the [S II] lines using the Fabry-Pérot interferometer with the CAFOS wide-field imager mounted on the 2.2 m telescope in Calar Alto. The data were obtained as part of a Director Discretionary Time program on 28 August 2009.

We obtained images centered in the Tr 37 globule, around the CTTS 14–141, RA(2000) Dec(2000) 21:36:49.41 +57:31:22.0, which showed remarkable variable forbidden line emission in our previous spectroscopic surveys. We obtained 3 dithered 600 s exposures with the Fabry-Pérot interferometer at 6716, 6730, and 6750 Å, resulting in narrow-band images centered on the two [S II] lines and a continuum observation with the same width in the line-free region around 6750 Å. An additional 3×10 s Johnsons *R* band image was also obtained for comparison. The data were reduced (bias, flat field) and combined according to the standard procedures using IRAF packages. Finally, a line-only image was obtained by subtracting the continuum 6750 Å

image from the [S II] ones. To improve the S/N, we combined both [S II] lines for the final result. We did not attempt any flux calibration, which is difficult due to the properties of the filter and to the fact that there is a wavelength drift over the CAFOS field. The resulting data clearly reveals several shocks in the field, not only associated to 14–141, but also to several of the protostars and embedded objects in the cloud (see Fig. 3).

3. Analysis

3.1. Spectral types and extinction

As a preliminary step to determine the membership and properties, we obtained spectral types for all the observed objects, which are listed in Table A.1. The spectral types of the objects with good S/N were derived using the combinations of indices employed for the classification of K-M3 stars in Cep OB2 by Sicilia-Aguilar et al. (2004), and a similar scheme for M3–M8 stars as it was used for classification of the Coronet cluster members (Sicilia-Aguilar et al. 2008). The classification of M3–M8 stars was based on the indices defined by Kirkpatrick et al. (1995), Martín et al. (1996), and Riddick et al. (2007). From the indices therein, we selected the best ones that did not suffer from strong problems due to atmospheric features, extinction, or lack of S/N in the blue (see Table 1). The calibration in Sicilia-Aguilar et al. (2004) is done in effective temperature (see Table 2). The effective temperatures (T_{eff} , in units of 10^3 K) are derived as $T_{\text{eff}} = T_0 + b \times (I - I_0)$, where I is the measured index, and T_0 , I_0 , and b are the zero-point values of effective temperature and index, and the slope of the relation resulting from the fit of several standard stars (Sicilia-Aguilar et al. 2004). The index I is obtained as a function of the flux in different wavelength ranges ($F_{\lambda_1-\lambda_2}$ is the flux between the wavelengths λ_1 and λ_2 in Å). The values of T_{eff} are transformed to spectral types using the calibration by Kenyon & Hartmann (1995). The spectral types of objects observed with SCORPIO were derived by direct comparison to standard stars, given their reduced wavelength coverage. We also note that since the SCORPIO spectra do not include the main features for classification of G/K stars, stars other than M-type observed by SCORPIO have very uncertain spectral types.

The indices are not applicable out of a given spectral range. Therefore, we did a preliminary visual classification of the stars as “earlier than G”, “GK-type”, and “M-type” before computing the spectral types. Due to our selection criteria, most of the stars found to be earlier than G are unlikely members, and they are simply listed in Table A.1 as “early type” (E). For the objects classified as “GK-type”, we used the MgI and CaI indices. The number of indices applicable to G-type and early-K stars is also very low, so the spectral types of objects earlier than K5 were refined by comparison to standard stars. For the objects classified as “M-type”, we used first the TiO 6185 index to determine whether the object was earlier or later than M3. For objects earlier than M3, we then used the CaI and TiO71 indices to refine the spectral type. For M3 or later types, we used the PC1, R1, and R3 indices to derive a preliminary spectral type, which was refined by using the TiO 8465, VOa, VOb, and PC2 indices, if within their applicable range. For each star, the final spectral type is calculated as the average of the types obtained with the applicable indices. In all cases, we performed a visual comparison with standard stars to check that the estimated spectral type is in agreement with the appearance of the spectrum. The few cases where there was a discrepancy between the derived type and the visual inspection could be tracked to different

Table 1. Indices used to derive the spectral type for stars later than M2.5.

Name	λ Numerator	λ Denominator	Range	Calibration	Reference
PC1	7030–7050	7525–7550	M3–M9	$-0.06 + 2.95 X$	1, 2, 4
PC2	7540–7580	7030–7050	M4–M8	$-0.63 + 3.89 X$	1, 2, 4
R1	8025–8130	8015–8025	M2.5–M8	$2.8078 + 21.085(X - 1.044) - 53.025(X - 1.044)^2 + 60.755(X - 1.044)$	3
R2	8415–8460	8460–8470	M3–M8	$2.9091 + 10.503(X - 1.035) - 14.105(X - 1.035)^2 + 8.5121(X - 1.035)$	3
R3	$(8125-8130) + (8415-8460)$	$(8015-8025) + (8460-8470)$	M2.5–M8	$2.8379 + 19.708(X - 1.035) - 47.679(X - 1.035)^2 + 52.531(X - 1.035)$	3
TiO 8465	8405–8425	8455–8475	M3–M8	$3.2147 + 8.7311(X - 1.085) - 10.142(X - 1.085)^2 + 5.6765(X - 1.085)$	3
VOa	$(7350-7370) + (7550-7570)$	7430–7470	M5–M9	$5.0705 + 11.226(x - 0.982) + 6.7099(x - 0.982)^2$	3
VOb	$(7860-7880) + (8080-8100)$	7960–8000	M4–M9	$3.4875 + 29.469(x - 1.017) - 156.53(x - 1.017)^2 + 394.28(x - 1.017) - 325.44(x - 1.017)^4$	3

Notes. Indices used for spectral typing of mid- and late-M type stars. The wavelengths are given in Å. In the calibration, X represents the index obtained by dividing the numerator and denominator, and the resulting number indicates the M subtype.

References. 1 = Kirkpatrick et al. (1995); 2 = Martín et al. (1996); 3 = Riddick et al. (2007). 4 = Sicilia-Aguilar et al. (2008).

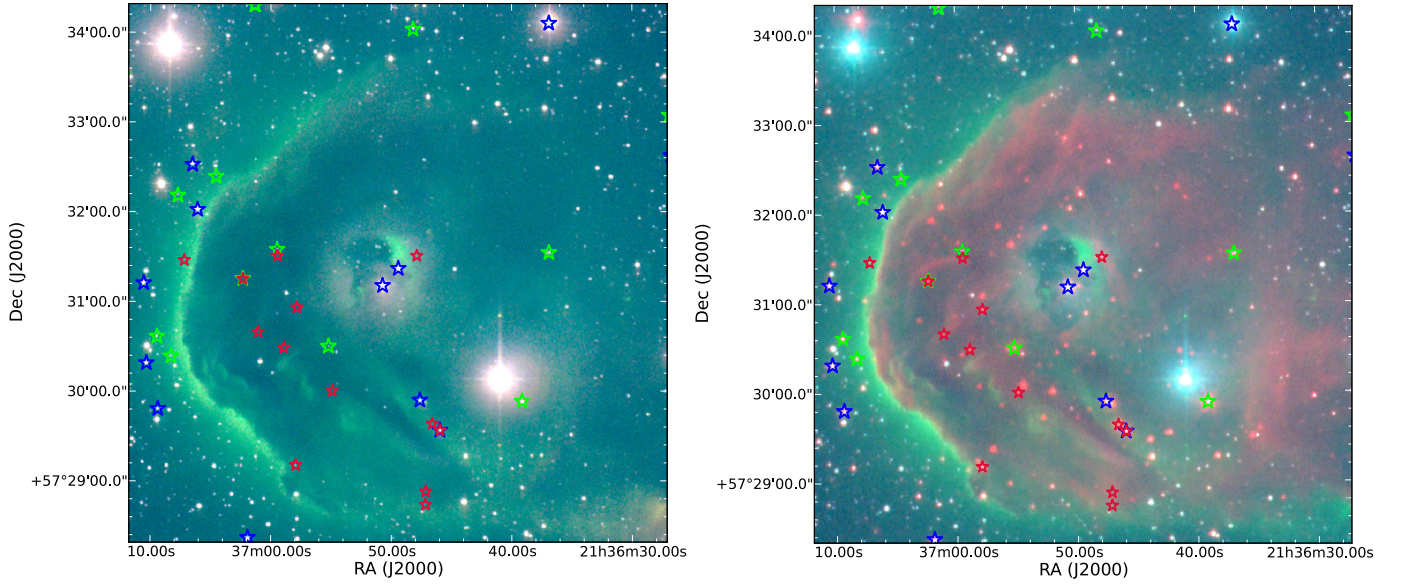


Fig. 3. Two 3-color images of the IC 1396 A globule. *Left:* narrow band at 6750 Å, [S II] combined at 6716 and 6730 Å, and *R* band as red, green, and blue, respectively. *Right:* IRAC1, [S II] combined at 6716 and 6730 Å, and *R* band as red, green, and blue, respectively. Known members detected via optical spectroscopy are marked as blue stars, new members are marked as green stars. *Spitzer* embedded candidates (SA06a) are marked by red stars.

Table 2. Indices used to derive the spectral type for G,K,M-type stars.

Name	T_0 (10 K)	I_0	b (10 K)	Range ($T_{\text{eff}}/10^3$ K, Spec. Type)	Index (I)
TiO 6185	3.40	1.58 ± 0.03	-0.94 ± 0.11	3–3.9, M5–M0	$F_{6165-6210}/F_{6100-6150}$
TiO 7140	3.40	1.99 ± 0.02	-0.40 ± 0.03	3–3.7, M5–M2	$F_{7125-7155}/F_{7020-7050}$
MgI	5.35	0.84 ± 0.02	5.50 ± 0.28	4.8–6, K2-G0	$(2 \times F_{5160-5180})/(F_{5005-5025} + F_{5225-5245})$
CaI	3.22	1.43 ± 0.01	-1.18 ± 0.05	3–3.6, M5–M3	$(F_{6000-6200} + F_{6300-6320})/(2 \times F_{6155-6175})$
CaI	4.10	1.16 ± 0.03	-8.74 ± 0.80	3.6–5.1, M3-K1	$(F_{6000-6200} + F_{6300-6320})/(2 \times F_{6155-6175})$

Notes. Indices used for spectral typing of G, K, and early-M star (Sicilia-Aguilar et al. 2004).

problems (presence of stellar or sky emission lines, lack of S/N in part of the spectrum, contamination by scattered light) that were addressed by removing the discrepant indices, and using the noncontaminated ones to derive the final spectral type.

In case of the objects with more than one spectra, we derived the spectral type for each one and consider the result of the best S/N spectrum (if the quality of both was very different). There is a very good agreement between all estimates (within 1–2 subtypes, depending on spectral type and data quality). Spectral types had been previously derived for 14 among the 17 objects in common with our previous campaigns. Among these, we recover the previous spectral type (± 1 subtype) in 9 cases, 2 cases are off by up to 2 subtypes, and 3 are off by up to 3 subtypes (corresponding mostly to faint M-type stars with low S/N in this or in previous surveys and/or limited spectral coverage). This confirms our typical estimated error of 1–2 subtypes, strongly depending on the S/N. In some cases, real spectroscopic variations were observed between 2009 and 2010, probably due to variations in the accretion activity and in the stellar spots. Two examples of this behavior are 213701319+573418289 (M3.0/M1.0, 2009 spectrum later than the 2010 one) and 213710877+573846877 (M4.5/M2.0, later in 2009).

We obtained the extinction of each object by comparing the observed optical data at VRI with the theoretical colors for young Taurus stars with the same spectral type (Kenyon & Hartmann 1995), and applying the relations of Cardelli et al. (1989) to derive A_V from $E(V - I)$ and $E(V - R)$

for the Johnsons filters. Whenever *VRI* photometry was available, we used both $E(V - I) = 0.521 A_V$ and $E(V - R) = 0.249 A_V$, estimating A_V as the average, with an error corresponding to the standard deviation. In the cases where one optical band was missing, we used the available data ($V - I$, $V - R$, or $R - I$) to compute the extinction, and estimated the error considering the typical spectral typing error. In the cases where no optical data (or only one optical band) were available, the extinction was derived from the 2MASS photometry, considering the theoretical colors from Bessell & Brett (1988) and the corresponding relations for $E(J - H) = 0.092 A_V$ and $E(H - K) = 0.076 A_V$. For the few objects that are confirmed to be members but have no reliable spectral types, we take the average cluster extinction ($A_V = 1.6$ mag; SA05). The final extinctions are listed in Table A.1.

3.2. Membership

The membership of the stars was established by a combination of several indicators. Typical youth indicators are the Li I absorption at 6708 Å and the $H\alpha$ equivalent width (EW). The EW of both $H\alpha$ and Li I are listed in Table A.1. Table A.5 lists other lines that have been observed in some members, mostly strongly accreting CTTS where the whole Balmer series is visible, together with the Ca II IR triplet, He I lines, Ca II H and K lines, and some Fe I and O I emission (Hamann & Persson 1992; Appenzeller et al. 2005), plus a few objects with forbidden [S II] and [O I] lines related to shocks (Hamann 1994). The

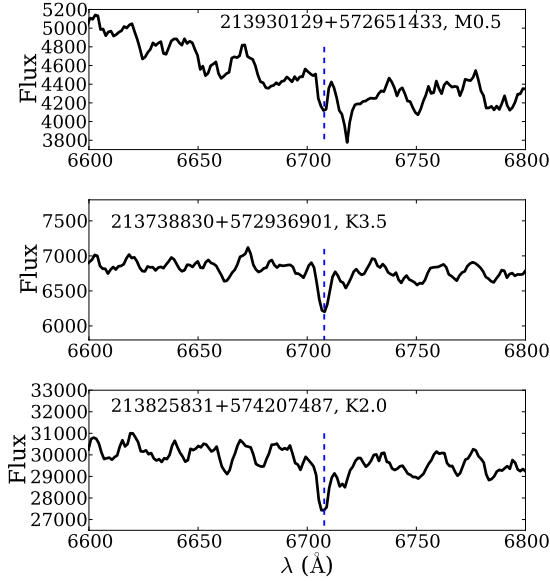


Fig. 4. Some examples of Li I detections with the MMT/Hectospec. The flux is in arbitrary instrumental units. The broad photospheric lines in 213825831+574207487 are also typical of a relatively fast rotator.

most reliable indicator of youth for late-type stars is the Li I absorption at 6708 Å (Fig. 4). Objects with clear Li I detection are labeled as sure members, and objects with good S/N at 6708 Å and no evidence of Li I absorption as labeled as nonmembers. Unfortunately, the Li I line is not always detectable in these faint objects, so we need additional membership criteria.

The H α line in emission is the main characteristic of T Tauri stars. In general, we followed the criteria of White & Basri (2003) regarding accretion and the distinction between classical and weak-line T Tauri stars (CTTS/WTTs). For the objects observed with the multifiber spectrograph Hectospec, sky subtraction is complicated due to the strong nebular emission in Tr 37, so low H α EW values are uncertain. Young, nonaccreting M-type stars can be hard to classify based on their H α emission since one of the main sources of contamination are older dMe stars in the field. Therefore, late-type stars with strong H α emission (>10 Å) were classified as members, especially if the *Spitzer* data show an excess consistent with a disk. Stars with weak H α emission (<10 Å) and no disk were considered as potential members, requiring additional information to confirm membership. Stars with H α absorption, especially those with late K or M spectral types², were rejected as nonmembers.

Our previous study of the solar-type stars revealed that the extinction towards Tr 37 is moderate, relatively constant over the cluster (except in the globules), and mostly due to foreground material. The distance of the cluster (870 pc, Contreras et al. 2002) imposes a minimum extinction around $A_V = 1$ mag, and the study of the solar-type population revealed an average extinction of $A_V = 1.56 \pm 0.55$ mag, with nearly all the bona-fide members outside the globule having $A_V < 3.5$ mag (SA05). This allows us to use the extinction as a further membership criterion, by defining the extinction ranges expected for the cluster members. Since this survey targeted fainter and thus potentially more extinguished members, we explored the extinction distribution of our newly found objects with Li I absorption

² Some early K and late G WTTs may have nearly zero emission, despite their youth, with the White & Basri (2003) criterion for CTTS being as low as H α EW > 3 Å.

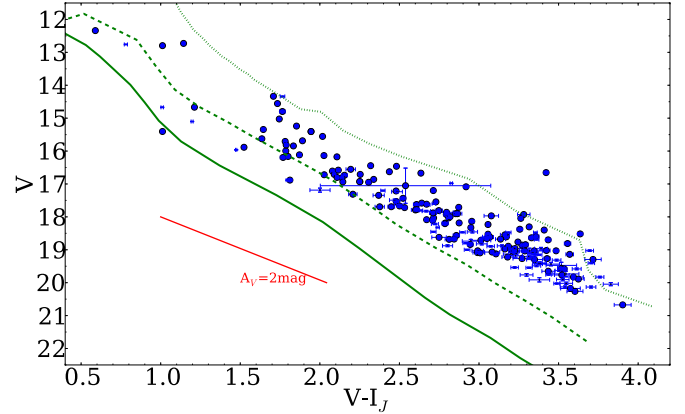


Fig. 5. V vs. V – I (Johnson system) diagram of the members (large filled circles) and probable members (small points) found in this survey. For comparison, the Siess et al. (2000) isochrones for 1, 10, and 100 Myr are displayed, transformed into the Johnsons system according to Fernie (1983) and Getman et al. (2012). An extinction vector (Cardelli et al. 1989) is also displayed, although they are often smaller than the symbols.

(42 in total). The average extinction and standard deviation is $A_V = 1.94 \pm 0.69$ mag. There are no Li I-detected members with $A_V > 4$ mag, and only 7% have extinctions ≥ 3.5 mag. There are also no Li I members with extinctions lower than 0.8 mag, and only 5% of the members have extinctions below 1 mag, while 29% have $A_V \geq 1.5$ mag. Therefore, we consider as candidate members all the objects with extinctions in the range 1–4 mags. Objects in this range with additional membership indicators (strong H α emission, IR emission from a disk) are considered as sure members, while objects with no additional indicators of youth (no Li I absorption, no disk, weak H α , but extinction consistent with the cluster values) are considered as probable members. Objects with extinctions out of the cluster range but strong indicators of membership (strong accretion-related lines and disk emission) are considered as members.

Finally, since this survey was fully independent of the X-ray observations of the IC 1396A globule by Getman et al. (2012), we also checked the objects in common with X-ray observations. A total of 23 of the X-ray YSO candidates and 16 of the non-Xray YSO with disks were found in common with our member selection, all labeled as sure and probable members. Four probable members with X-ray detections were thus upgraded to sure members. Three further objects (one probable member, two probably nonmembers) were listed among uncertain X-ray detections, and we are keeping their original membership classification.

Placing the new members and probable members in the V vs. V – I diagram (Fig. 5), we find that their ages are consistent with the mean age of 4 Myr derived previously (SA05). Since the Siess et al. isochrones are given in the Cousins system, we transformed them into the Johnsons system following the prescriptions of Fernie (1983, for blue stars, $V - I_c < 1.5$ mag), and Getman et al. (2012, for red stars, $V - I_c > 1.5$ mag). A few of the objects appear below the 10 Myr isochrone, but in most cases they are stars with flared disks and high (or even anomalous) extinction being thus probably UXor candidates (all labeled in Table A.1). In addition, early K and G stars tend to deviate from typical isochrone models, probably due birthline uncertainties (Hartmann 2003). Some of the probable members that have anomalous positions in the V vs. V – I diagram may be

contaminants, giving us an idea of the uncertainty in the membership of the objects marked with “P”.

Taking into account the five different criteria (Li I absorption, $H\alpha$ emission, disk excess, extinction, and X-ray), from the initial collection of 565 objects observed, we arrive to a collection of 141 sure members, plus 64 probable members and 33 probable nonmembers. The rest of the 308 observed stars are rejected as nonmembers or marked as uncertain cases on the basis of low S/N (19 in total). A total of 28 identified members are in common with the $H\alpha$ survey of Barentsen et al. (2011), and 17 objects corresponded to re-observations of previously identified members in SA05 and SA06b³. One further object was suggested to be a YSO by Morales-Calderón et al. (2009). Excluding the objects that had been previously suggested to be members by the different authors, we arrive to 78 newly identified members and 64 probable members (to be confirmed with future followup observations), mostly M-type stars and GK members with extinctions higher than the cluster average and with protoplanetary disks.

4. Discussion

4.1. Disk structure and the accretion/disk connection

As we had found in our previous papers (SA06a; Sicilia-Aguilar et al. 2007), there is a large variety of disk morphologies in Tr 37. We have classified the new disks following the scheme developed in our *Spitzer* IRS-based study (SA11). The main criteria for defining the disk evolutionary state are the presence of inside-out evolution, as in transitional and pre-transitional disks, and the evidence of generalized small-dust depletion, as in homologously depleted disks (Currie et al. 2009). A comparison of the disk slope at short and long wavelengths is fundamental to distinguish disks with evidence of inside-out evolution, although the silicate feature at $10\ \mu\text{m}$ also plays an important role. Objects with inner gaps or partially cleared disks, such as pre-transitional disks (Espaillat et al. 2010), have weak near-IR fluxes, strong silicate features, and strong mid-IR excesses, are especially hard to identify without spectroscopic information. Low fluxes at $24\ \mu\text{m}$ and longer wavelengths are a key to identify small-dust-depleted disks.

To quantify inner disk evolution, we consider $\alpha(\lambda_1 - \lambda_2)$, defined as the SED slope between two wavelengths:

$$\alpha(\lambda_1 - \lambda_2) = \frac{\log(\lambda_1 F_{\lambda_1}) - \log(\lambda_2 F_{\lambda_2})}{\log \lambda_1 - \log \lambda_2}. \quad (1)$$

Objects with nearly photospheric colors ($[3.6]-[4.5] < 0.2$ mag, $\alpha(3.6-4.5) \sim -3.0$ – -2.13) but significant excess at longer wavelengths are classified as transition disks (TD). Disks with moderate to low near-IR excess ($[3.6]-[4.5] \sim 0.2$ – 0.4 mag, $\alpha(3.6-4.5) \sim -2.13$ – -1.30) and a change in the sign of the slope between 8 – 12 and $24\ \mu\text{m}$ are labeled as “kink” disks (according to SA06a terminology) and are good candidates for pre-transitional disks (PTD).

Regarding the small-dust mass, and based on our previous results (SA11), we consider objects with low IR fluxes at all wavelengths and reduced $24\ \mu\text{m}$ fluxes as globally dust-depleted disks. Dust-depleted disks have near-IR in the PTD range or

lower, but with similarly steep slopes at all other wavelengths and thus very low $24\ \mu\text{m}$ fluxes (for K- and M-type stars, $\lambda F_{\lambda} \leq 2-3 \times 10^{-13}$ erg cm⁻² s⁻¹). We labeled the objects in Table A.3 according to the disk classification. Figure 6 is color-coded to show the different disk types vs. the SED slopes at different wavelengths. The final classification also requires visual inspection of all the SEDs to detect the few cases that satisfy the mentioned criteria but display SEDs that evidently do not correspond to the presumed disk class. Objects with uncertain photometry/excesses are also excluded from the following analysis and discussion.

Several studies have suggested a strong connection between the IR excesses typical of protoplanetary disks and active accretion (e.g. Sicilia-Aguilar et al. 2006b, 2010; Fedele et al. 2010) while some others suggested that the differences between nonaccreting, WTTS and CTTS in terms of disks are minimal (e.g. Cieza et al. 2007; Oliveira et al. 2013). Differences in accretion between transitional and nontransitional disks have also been matter of debate (Najita et al. 2007; Muzerolle et al. 2010; Sicilia-Aguilar et al. 2010; Fang et al. 2009, 2013b; Merín et al. 2010). Tr 37 is an interesting region, having a large number of disks with signs of evolution and a disk fraction slightly below 50% (SA06a). A first approach including all known low-mass stars with spectral types G, K, M, suggests a high correlation between the $H\alpha$ EW, the SED slopes, and our disk classification (Fig. 7; the disk classification is shown in the color-code). Figure 8 displays the $H\alpha$ EW vs. the effective temperatures (T_{eff}) for the whole sample of low-mass members, also color-coded according to their disk types. Instead of separating the objects in CTTS/WTTS according to their $H\alpha$ EW, we directly considered the measured $H\alpha$ EW within each disk class, and performed a double-side Kolmogorov-Smirnov (KS) test to find out the probability that the $H\alpha$ EW of different types of objects are drawn from the same sample.

Table 3 summarizes the results of the KS test. We find unmistakable evidence of a different distribution of $H\alpha$ EW between objects with disks (including all types of disks) and without disks (no evidence of excess emission at any wavelength), with probabilities nominally 0 that both distributions are drawn from the same sample. We also find significant differences between the $H\alpha$ EW of TD and full-disks, mostly related to the fact that between 40 and 60% of the TD have $H\alpha$ values consistent with nonaccreting stars⁴, while this is extremely rare among full-disks. Fang et al. (2009, 2013b) found that the fraction of strong accretors ($H\alpha$ EW $> 2 \times H\alpha_{\text{threshold}}$ for a given spectral type) in the Orion Lynds 1641 and 1630N clouds is around 60% among full disks, while only 21–26% of the TD have comparable high accretion. Fang et al. (2013b) inventoried a sample of ~ 1390 YSOs in Lynds 1641. Their sample includes more than 60 PTD/TD objects which have observed with spectroscopy measuring $H\alpha$ EW. Among their PTD/TD sample, 36 objects can be classified as TD, and 25 sources as PTDs according to our criteria. The fractions of accretors in both samples are $42 \pm 11\%$ and $52 \pm 14\%$, respectively. Therefore, the results in the Orion Lynds clouds are consistent with Tr 37.

Dust-depleted disks have also significantly lower $H\alpha$ EW, and thus significantly lower accretion rates (sometimes consistent with no accretion) than normal full-disks. This supports the idea of a strong connection between gas and dust evolution,

³ These include 11–1499, which was labeled as probably nonmember following the criteria in this study, but had Li I absorption in our better S/N spectra from SA05 and X-ray emission according to Getman et al. (2012), so we consider it as member, and the previously identified probable member 21–851, now rejected as cluster member.

⁴ Note that although $H\alpha$ EW is a good indicator of accretion, further data like high-resolution $H\alpha$ spectroscopy or U band photometry is needed to rule out cases with very low accretion rates.

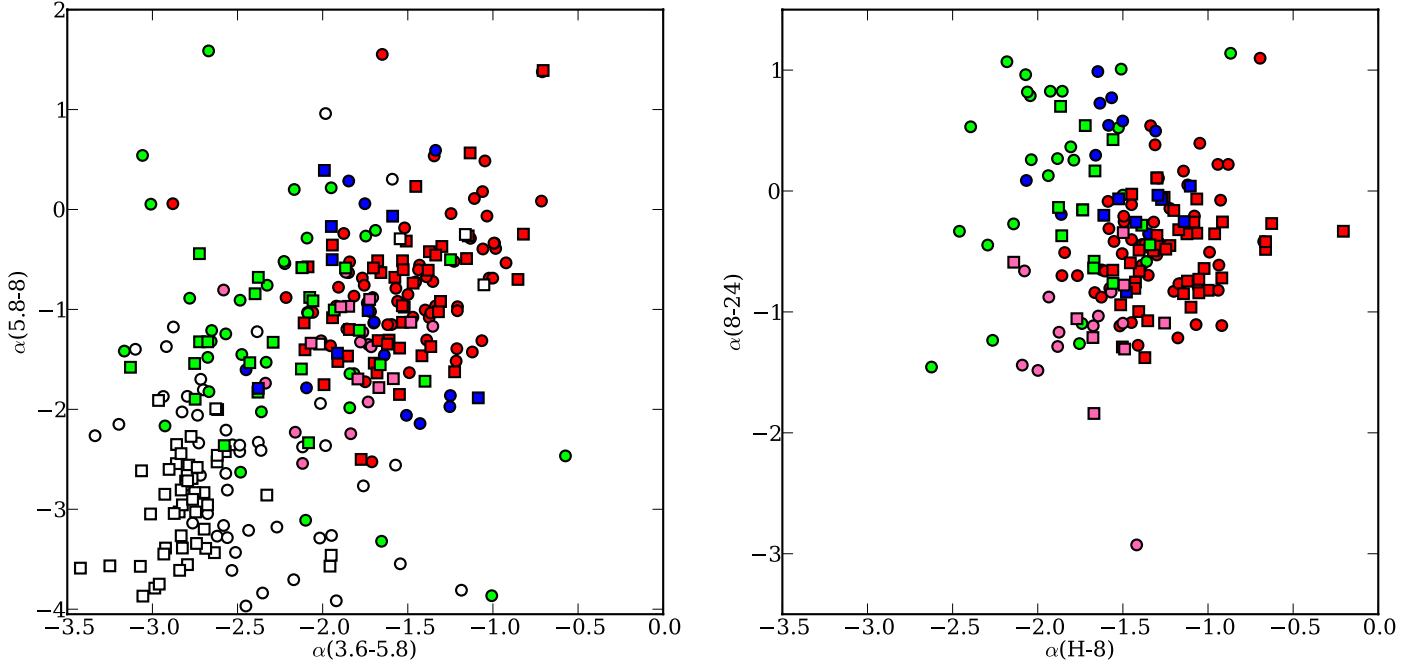


Fig. 6. Different disk slopes for the objects with different spectral types. Circles mark the newly identified members, squares denote the previously known ones. Diskless objects are open symbols (none of the diskless objects is detected at $24 \mu\text{m}$, and in general diskless objects with apparent excesses are due to contamination and/or uncertain photometry). Red symbols are the typical full-disks. Green symbols mark the TD. Blue symbols mark the PTD. Pink symbols mark the dust-depleted disks.

Table 3. Results of the double-sided KS probability test for the $H\alpha$ EW for objects with different types of disks.

Disk types	2006 sample	2013 sample	All objects	M-type	G/K-type	Comments
Full-disks/Diskless	1E-17	6E-8	1E-22	7E-12	2E-11	Strong difference
Full-disks/PTD	0.47	0.63	0.28	0.62	0.57	No significant difference
Full-disks/TD	0.0001	0.02	5E-6	0.009	5E-5	Significant difference
Full-disks/Depleted	0.07	0.004	3E-4	0.001	0.24 ^a	Significant difference (only M-type stars)
Diskless/PTD	1E-5	4E-4	1E-8	1E-5	5E-4	Strong difference
Diskless/TD	0.007	0.07	0.001	0.0001	0.28	Significant difference (only M-type stars)
Diskless/Depleted	0.006	0.61	0.16	0.82	0.005 ^a	Potential difference (only G/K stars)
Disked/Diskless	1E-14	4E-6	4E-18	2E-10	1E-8	Strong difference

Notes. The 2006 sample corresponds to the members identified in our previous work, the 2013 sample includes the newly detected objects in this work. ^(a) Small number statistics, only 6 depleted disks among G/K stars.

where both signs of inside-out evolution (in TD) and global dust depletion appear to be related to lower accretion rates. Observations of evolved disks and accretion signatures in older clusters, like γ Velorum (Hernández et al. 2008; Jeffries et al. 2009) and η Cha (Lawson et al. 2004; Bouwman et al. 2006; Sicilia-Aguilar et al. 2009) show that, despite the differences in environment and disk classes, there is a clear trend for evolved disks to display reduced or even zero accretion rates, consistent with parallel dust and gas evolution. On the other hand, the $H\alpha$ EW and thus the accretion rates of PTD and full-disks are not significantly different. This is remarkable, since PTD are good candidates to host clean gaps in their disks, maybe related to planet formation (Espaillat et al. 2010). It could be due to difficulties to identify disks with gaps from unresolved observations and lacking spectra of the $10 \mu\text{m}$ region, or be a direct consequence of most of the full-disks in Tr 37 having moderate accretion rates, compared to younger regions like Taurus (SA06b; Sicilia-Aguilar et al. 2010). Although half of the TD have $H\alpha$ EW consistent with no accretion, and most of the dust-depleted disks also show relatively low $H\alpha$ EW, the difference

between disked and diskless objects is still remarkable even if TD and dust-depleted disks are included.

We also explored whether the differences in accretion vs. disk type depend on the spectral type. Table 3 reveals that the differences are subtle. Non-accreting TD seem to be more frequent around G/K-type stars. One explanation could be that for a given excess, the holes in a G/K-type star will be much larger than in M-type objects, although it could also indicate that accretion can survive for longer time in the disks around M-type objects, once the inner disk starts dispersing. The data also suggests that M-type dust depleted disks are consistent with no accretion, which is in agreement with our observations of M-type stars in the Coronet cluster (Sicilia-Aguilar et al. 2008, 2011a). Nevertheless, a remarkable difference is that while most of the disks around M-type stars in the Coronet cluster are dust-depleted or have very low disk mass compared to their stellar mass ($M_d/M_* < 10^{-4}$; Sicilia-Aguilar et al. 2013), strongly dust-depleted disks are a minority among M-type stars in Tr 37, at least considering our detection limits at $24 \mu\text{m}$. In general, the differences in accretion and disk structure between G-K type and

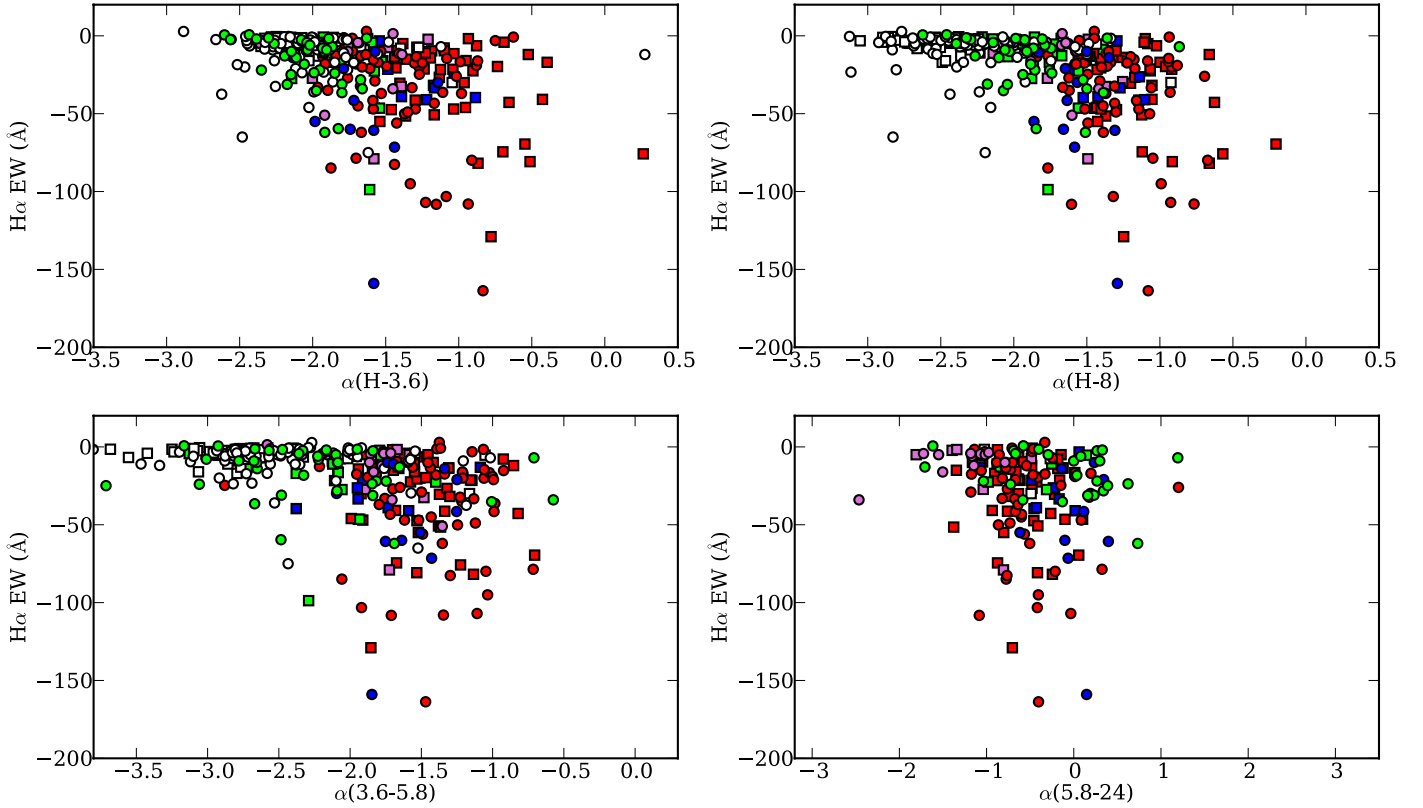


Fig. 7. $H\alpha$ EW vs. disk slope for the members of Tr 37. Known members from previous work are marked as squares (SA05,SA06a,b). New sure members from this work are displayed as circles. Diskless stars are open symbols, typical full-disks are colored in red, PTD are marked in blue, TD are colored in green, and dust-depleted objects appear in pink.

M-type stars are smaller in Tr 37 than observed in the Coronet cluster (Currie & Sicilia-Aguilar 2011).

4.2. Radiative transfer models of the disks

To extract quantitative information from our previous disk structure classification, we followed the scheme in SA11, using the RADMC radiative transfer code (Dullemond & Dominik 2004) to model a subset of the disks within each class (normal full-disks, PTD, TD, and dust depleted disks). The basic parameters in the RADMC code are the inner disk radius, the outer disk radius (R_{disk}), the disk vertical scale height, and the dust distribution. The inner disk radius is set to the place where the temperature is 1500 K, approximately the dust sublimation radius, and the outer disk radius is taken to be 100 AU, although our data offers a poor constrain on this parameter and there is substantial degeneracy between disk radius and total disk mass. The disk vertical scale height is given as $H/R \propto R^{1/7}$, although we also computed the scale given by hydrostatic equilibrium. Finally, the dust distribution is taken to be a collisional power law with exponent -3.5 , between a typical minimum size of $0.1 \mu\text{m}$ and a typical maximum size of $100\text{--}10000 \mu\text{m}$. The gas to dust ratio is 100, and gas and dust are always assumed to be well-mixed, with all dust grains having the same temperature distribution. The stellar parameters (mass, radius) are derived from the optical data and spectral types, using the transformations in Siess et al. (2000) and Kenyon & Hartmann (1995). The dust is considered as amorphous silicate dust with equal amount of magnesium and iron (Jäger et al. 1994; Dorschner et al. 1995⁵). We also include

25% of carbon grains with the same size distribution than the silicate dust. The SEDs are calculated for an intermediate disk inclination (45 degrees), although for these relatively flat disks, there is little difference unless the disk is viewed edge-on.

As in our previous papers, our models are not aimed at a perfect reconstruction of the SED, but at exploring the parameter space. Starting with the most simplified model possible, we check whether any structural differences are required to obtain SEDs similar to the ones we observe by varying only the disk mass and the vertical scale height (with values not far from hydrostatic equilibrium). Only if no reasonable fit is attained in this way, we proceed to change the inner disk radius, the dust grain distribution (reducing the content of small dust grains or increasing the maximum grain size), and also to introduce radial variations in the vertical structure and/or the dust composition. There is a very strong degeneracy between the flaring of the outer disk, the total disk mass, the grain distributions in the inner and outer disk, and the radius (or disk temperature) at which the disk properties (flaring, density, grain size distribution) change. Constraining the precise properties of individual disks with unresolved observations is highly degenerated, so our purpose is to prove that a simple disk structure cannot reproduce the observed SEDs for TD and PTD, unless some radial changes are included, even if the precise values of the varying parameters cannot be determined. Table 4 summarizes the model disk parameters within each disk class. A brief discussion on each class and the most appropriate models follows.

4.2.1. The typical full-disks

The full-disks (Fig. 9) are easy to reproduce by regulating the disk mass to fit the $24 \mu\text{m}$ point, and changing the vertical scale

⁵ See <http://www.astro.uni-jena.de/Laboratory/OCDB/newsilicates.html>

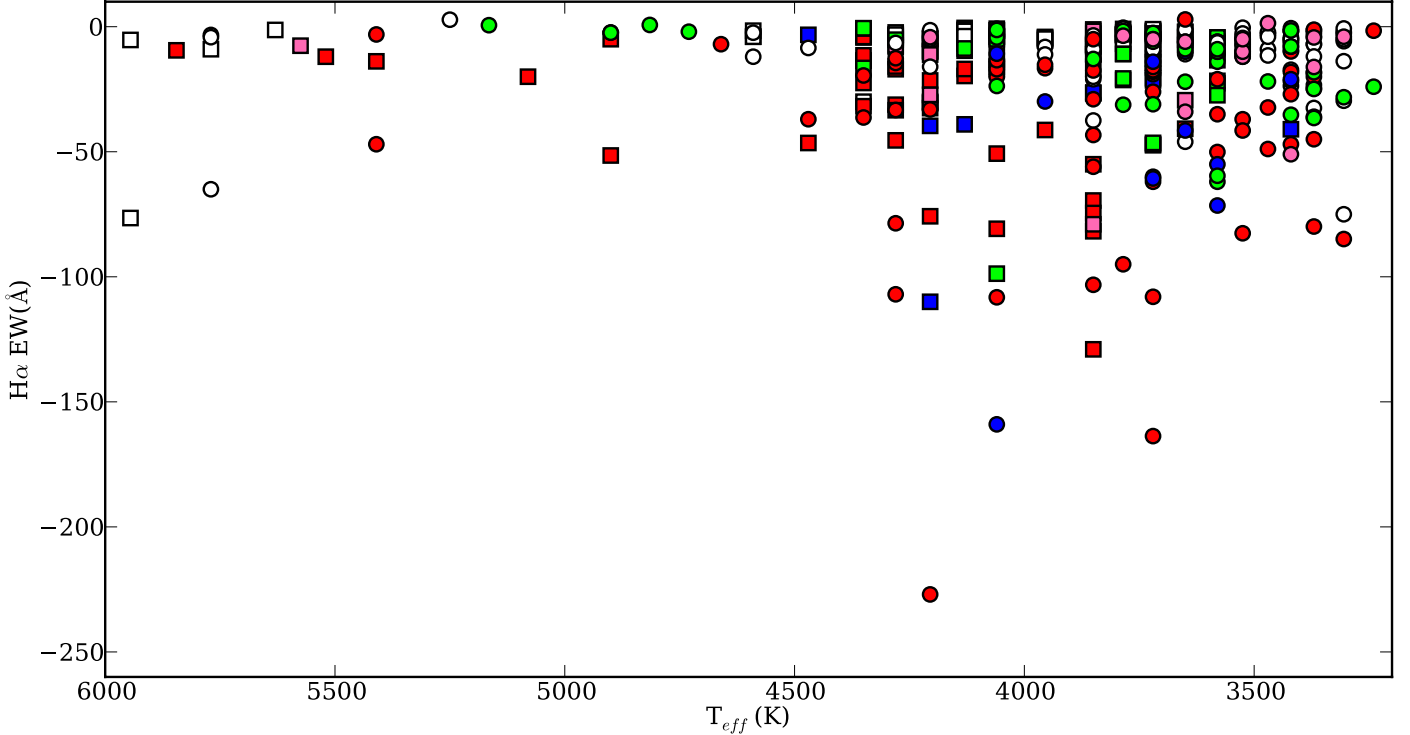


Fig. 8. $H\alpha$ EW vs. effective temperature for the objects with different types of disks. Squares denote the stars observed in our previous programs, while new members from this work are marked by circles. Diskless stars are open symbols, full-disks are colored in red, PTD are marked in blue, TD are colored in green, and dust-depleted objects appear in pink.

height, either assuming a global power law for the disk flaring at all radii or hydrostatic equilibrium. The required vertical scale heights do not depart much from hydrostatic equilibrium, although we find disks that appear higher than predicted by hydrostatic equilibrium (especially, among the higher mass disks) while other disks tend to be flatter, as expected from dust settling. We modeled three objects, with different spectral types and different disk masses, 213659108+573905636, 213751210+572436151, and 213823950+572736175, in representation of this broad and numerous class.

Disks with large excesses, like 213659108+573905636, require a very large amount of mass in small dust grains. Although the maximum grain size is unconstrained, if we assume a collisional distribution with maximum grain sizes over $100 \mu\text{m}$ and a gas to dust fraction of 100, we would require disk masses about 10% of the estimated stellar mass. This would be on the upper limit according to submillimeter and millimeter observations (Andrews & Williams 2005, 2007). On the other hand, disks like that around 213823950+572736175, with a low-to-moderate mass, probably require large grains to account for mass enough to sustain the accretion rates we expect from their strong $H\alpha$ emission.

Other disks have very strong near-IR excesses but a lower $24 \mu\text{m}$ than expected, suggestive of strong flaring but a very low dust mass, even if we consider substantial grain growth (e.g. 213751210+572436151, 213809997+572352782). This is similar to other disks in the Coronet cluster (CrA-159 and HBC 677; Sicilia-Aguilar et al. 2013). Further observations at longer wavelengths are needed to clarify the total dust content and other special structures that could affect their morphology, like truncation or gaps at larger radii. As a first approach, we consider these disks within the full-disk class.

4.2.2. The pre-transitional disks

The pre-transitional disks (Fig. 10) are the hardest class to identify with our available data. The lack of a mid-IR spectrum and information on the silicate feature are a strong constraint to identify disks with partially optically thin regions in their inner disks (Espaillat et al. 2010; SA11). Nevertheless, the high $8\text{--}12 \mu\text{m}$ fluxes and sharp kinks in the mid-IR suggest disks where the properties in the innermost and outer disk change. Our models do not include gaps, although a gap created by a companion or by photoevaporation can offer a natural barrier to explain the radial changes in properties. Since this class is the most problematic, we selected 6 objects as examples (213658737+573848181, 213734649+571657705, 213929250+572530299, 213929408+570630605, 213945201+574912946, 213954058+572933454) and ran different models to show the degeneration of the various parameters. Our list of models is far from complete, but it shows that, despite the degeneracy, the SEDs reveal that some radial variations in disk properties are needed. The radial changes, reflected in Table 4, are a signature of a distinct inner and outer disk, with different flaring, inner radius, grain sizes, and mass.

The case of 213734649+571657705 shows that a simple full-disk model fails to both reproduce the inner and outer disk properties (dashed line in Fig. 10), while a change in grain size distribution and flaring offers a good compromise to reproduce the SED (bold line). 213945201+574912946 offers a practical example of the impossibility to fit a pre-transitional SED with a simple full-disk model (dashed line), that would require extreme flattening far beyond hydrostatic equilibrium and a very large mass to account for the turn up at $24 \mu\text{m}$, but would still overestimate the fluxes at $8\text{--}12 \mu\text{m}$. A model with a differentiated inner disk and hydrostatic equilibrium comes close to the result

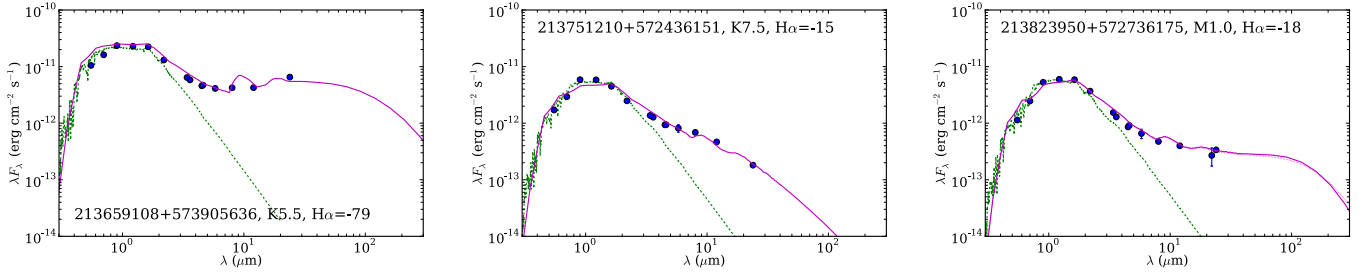


Fig. 9. Disk models for selected SEDs of typical full-disks (magenta lines). See Table 4 for information on the individual models. For comparison, the photosphere of a star with the same spectral type from the MARCS models (Gustafsson et al. 2008) is displayed. All datapoints have been extinction-corrected according to their individual values of A_V and assuming a standard extinction law (see Table A.1). Information about the $H\alpha$ EW (in \AA) is also displayed.

(dotted line), but we note that the best fit is attained by assuming the inner disk has a larger vertical scale height than predicted by hydrostatic equilibrium (bold line).

4.2.3. The transitional disks

For transitional disks (Fig. 11), we have evidence for an inner hole that is most likely devoid of small dust. We constructed models for objects with different spectral types and different hole sizes, parameterized by the temperature of the inner disk rim. As for pre-transitional disks, there is a great degeneracy between disk scale height, dust composition, and size of the hole, although the low near-IR fluxes cannot be explained without cutting the dust distribution at a temperature significantly lower than the dust destruction temperature (see for instance the large grain model for 213756779+573448171, which fails to reproduce the low near-IR fluxes).

Without information on silicate emission it is hard to constrain the minimum grain size. Dust distributions with larger minimum size grains produce lower near-IR emission. The total disk mass is also highly dependent on the outer disk radius and on the vertical scale height. Some of the disks could be close to hydrostatic equilibrium, with only minimal differences in some cases (e.g. 213633647+573517477). In others, the strong excesses require a vertical scale height over the hydrostatic equilibrium (e.g. 213735713+573258349), or the weak emission asks for a reduced vertical scale height (e.g. 213756779+573448171). The mass of certain TD, even assuming a significant grain growth, is well below $10^{-4} M_*$, which means that they also appear to be substantially dust-depleted (e.g. 213914837+573756779). Nevertheless, the main difference with this class, as we explain in 4.2.4, is that not all dust-depleted disks need to have an inner hole, and not all TD need to have very low small-dust-grain masses.

4.2.4. The dust depleted disks

Dust-depleted disks (Fig. 12) are also relatively simple. They can be reproduced with model without radial variations, but require a very low small dust mass (at least, with very low mass in the submicron to 20–30 μm range) and/or very strong settling. There is a strong degeneracy between mass and vertical scale height. In general, if we assume that the dust-depleted disks are in hydrostatic equilibrium, we require a total mass several orders of magnitude below the typical values of normal full-disks. If we impose strong settling and disk flattening, the small dust grain depletion does not need to be so dramatic, although in general an increase of mass over one order of magnitude (for the same

grain size distribution) cannot be compensated by flattening the disk, since the 24 μm fluxes would increase far beyond what is observed (e.g. 213030129+572651433). Some of the depleted disks may also have inner holes; 213854760+572450268 is one example where the failure of various models to reproduce simultaneously the 24 and 8 μm flux may indicate the presence of a small hole. However, this is not always necessary and most of them do not satisfy the criteria for TD.

The mass of the disk also depends strongly on the disk radius and on the maximum grain size, but even assuming millimeter-sized maximum grain sizes requires a very low mass for the disk, compared to typical full-disk values (see for instance 213733557+573550931). This implies that even if our data does not allow us to fully rule out a total higher disk mass in the disks classified as dust-depleted, the mass content in grains smaller than 20–30 μm needs to be very low, which is in any case a strong sign of evolution. From the analysis in Sect. 4.1, the dust depleted disks clearly show accretion differences with respect to full disks. Therefore, despite the degeneracy between disk mass and disk flaring/settling, which has also been discussed in the literature (e.g. Espaillat et al. 2012), our study suggests that these disks are in a different evolutionary stage from typical full disks. Even if we cannot constrain the mass of the disks, and even if the case is particularly hard for M-type stars that have naturally lower near-IR excesses, the low probabilities that M-type dust depleted disks and M-type full disks are drawn from the same collection of objects, and the fact that M-type dust depleted disks and M-type diskless stars are consistent with the same $H\alpha$ values (see Table 3) strongly point to a different evolutionary status compared to full disks. Accretion termination/gas depletion may be a sign of parallel dust and gas evolution, and also favor stronger dust settling within the disk. The study of silicate features (as in the case of 01–580; Sicilia-Aguilar et al. 2011a), and far-IR/submillimeter observations are a key to better constrain the disk mass of these objects, their structure, and the presence of settling (see for instance the models for 213930129+572651433 and 213944898+573537212).

4.3. What drives disk evolution and dispersal in Tr 37? Clues from accretion, dust, and environment

Putting together the members found in our previous papers and the newly found ones, we sum up to 361 low-mass (spectral types G, K, M) members in Tr 37. The current results are consistent with our previous estimates of the disk frequency ($48 \pm 5\%$, including all objects with excesses down to 24 μm , SA06a), although since this survey was strongly biased towards objects with disks, we cannot re-estimate the disk fraction.

Table 4. Disk models for selected members, according to their disk structure.

Object	T_{eff} (K)	R_* (R_{\odot})	M_* (M_{\odot})	M_{disk} (M_{\odot})	$a_{\text{min}}-a_{\text{max}}$ (μm)	$H_{\text{disk}}/R_{\text{disk}}$	$T(R_{\text{in}})$ (K)	Comments/model reference in plots
Full-disks								
213659108	4330	1.49	1.0	0.08	0.1–100	0.12	1500	Very massive, rich in small dust (bold line)
213751210	3955	0.80	0.7	2.4E–5	0.1–10000	0.25	1500	Very low-mass, maybe smaller radius? (bold line)
213823950	3729	0.92	0.6	2.9E–4	0.1–100	0.15	1500	Normal-to-low disk mass, mass depends on grain size (bold line)
"	3729	0.92	0.6	2.4E–3	0.1–10000	0.15	1500	Normal-to-low disk mass, mass depends on grain size (dashed line)
PTD								
213658737	3500	1.40	0.3	3.0E–3	0.1–100	0.13/0.22	1500/120	Less flared, less dense inner disk (bold line)
213734649	3720	1.00	0.45	4.5E–4	0.1–2/0.1–100	0.15/0.20	1500/300	Change in grain distribution inner/outer disk (bold line)
"	3720	1.00	0.45	4.5E–4	0.1–100	0.16	1500	Cannot fit mid-IR and near-IR properly (dashed line)
213929250	3720	1.00	0.40	2.0E–4	0.1–2/0.1–100	0.16/0.18	1500/400	Radial change in grain size and vertical scale height (bold line)
213929408	4060	1.15	0.80	8.0E–4	0.1–2/0.1–100	0.13/0.12	1500/200	Optically thin, small-grain inner disk (bold line)
213945201	4060	1.40	0.80	0.04	0.1–100	0.07	1500	An extreme attempt to fit with a uniform disk model (dashed line)
"	4060	1.40	0.80	6.4E–4	0.1–100	hydro	1500/200	Needs more flaring in inner part (dotted line)
"	4060	1.40	0.80	4.8E–4	0.1–100	0.13/0.11	1500/200	Best with puffed inner disk (bold line)
213954058	3960	1.10	0.80	4.0E–4	0.1–100	0.14/0.23	1500/150	Needs a thin inner disk and a thick, flared outer disk (bold line)
TD								
213633647	5165	2.90	2.00	4.0E–6	20–1000	0.32/hydro	500	No small dust, inner hole (dashed line)
"	5165	2.90	2.00	9.6E–8	0.1–100	0.32	500	Small grains, lower mass, silicate feature (bold line)
213735713	3580	1.10	0.35	7.0E–5	0.1–10000	0.20	250	Low mass, low $T(R_{\text{in}})$, high vertical scale height (bold line)
213756779	3650	0.75	0.40	1.6E–5	0.1–10000	0.15	350	Low mass, inner hole (bold line)
"	3650	0.75	0.40	1.2E–4	20–10000	0.08	1500	Low scale height, large grains, no hole, too much near-IR excess (dashed line)
213914837	3850	1.05	0.50	2.5E–7	0.1–100	0.06	1500	Small grains, very low mass, overpredicts 8–12 μm excess (bold line)
"	3850	1.05	0.50	4.0E–6	20–1000	0.06	1500	No small grains, better fit to 8–12 μm but still high (dashed line)
"	3850	1.05	0.50	3.0E–6	20–1000	0.06	800	Best fit includes small hole (dotted line)
Depleted								
213733557	3700	0.80	0.50	1.5E–6	0.1–100	0.12	1500	Without strong grain growth, very low mass (bold line)
"	3700	0.80	0.50	1.5E–5	0.1–10000	0.12	1500	Larger grain size, higher mass, but still depleted (dotted line)
213854760	3720	1.90	0.40	8.0E–5	20–1000	0.06	1500	Too much 8–12 μm excess (bold line)
"	3720	1.90	0.40	2.0E–6	0.1–100	0.05	1500	Extremely low vertical scale height underpredicts 24 μm (dashed line)
"	3720	1.90	0.40	8.0E–5	20–1000	hydro	1500	Hydrostatic equilibrium overpredicts 8–12 μm excess (dotted line)
213930129	3785	1.69	0.70	7.0E–4	0.1–100	0.05	1500	Very settled disk with small grains (bold line)
"	3785	1.69	0.70	5.6E–6	0.1–100	0.08	1500	Lower mass disk, close to hydrostatic equilibrium (dashed line)
"	3785	1.69	0.70	4.9E–6	0.1–100	hydro	1500	Hydrostatic equilibrium, lower disk mass (dotted line)
213944898	3500	1.21	0.26	1.3E–5	0.1–100	0.08	1500	Very settled disk with low mass still has too much mid-IR excess (dashed line)
"	3500	1.21	0.26	3.9E–6	0.1–100	0.10	1500	Lower mass, higher vertical scale height (bold line)
"	3500	1.21	0.26	3.9E–5	0.1–10000	0.10	1500	If strong grain growth is assumed, the mass may be higher (black dotted line)

Notes. The comments also include a reference to the models plotted in the figures. RADMC disk models for selected members with different disk structures (normal full-disks, pre-transitional disks [PTD], transitional disks [TD], and dust-depleted disks [Depleted]). The names of the objects have been shortened to fit the table. The stellar parameters (T_{eff} , R_*) are determined from the optical observations and spectroscopy. The disk parameters are modified to reproduce the observed SED in the whole wavelength range, starting with the simplest possible model (see Sect. 4.2). The disk masses are estimated assuming a gas-to-dust ratio of 100 and a collisional distribution for the dust with grain sizes $a_{\text{min}}-a_{\text{max}}$. The outer disk radius is taken to be 100 in all cases. A larger radius would also result in a larger dust mass. For pre-transitional disks with physically different inner and outer disks, we give the grain distributions, vertical scale height, and inner rim temperature for both the inner and the outer disk. In case of different models, the comments include a reference to the appropriate figure.

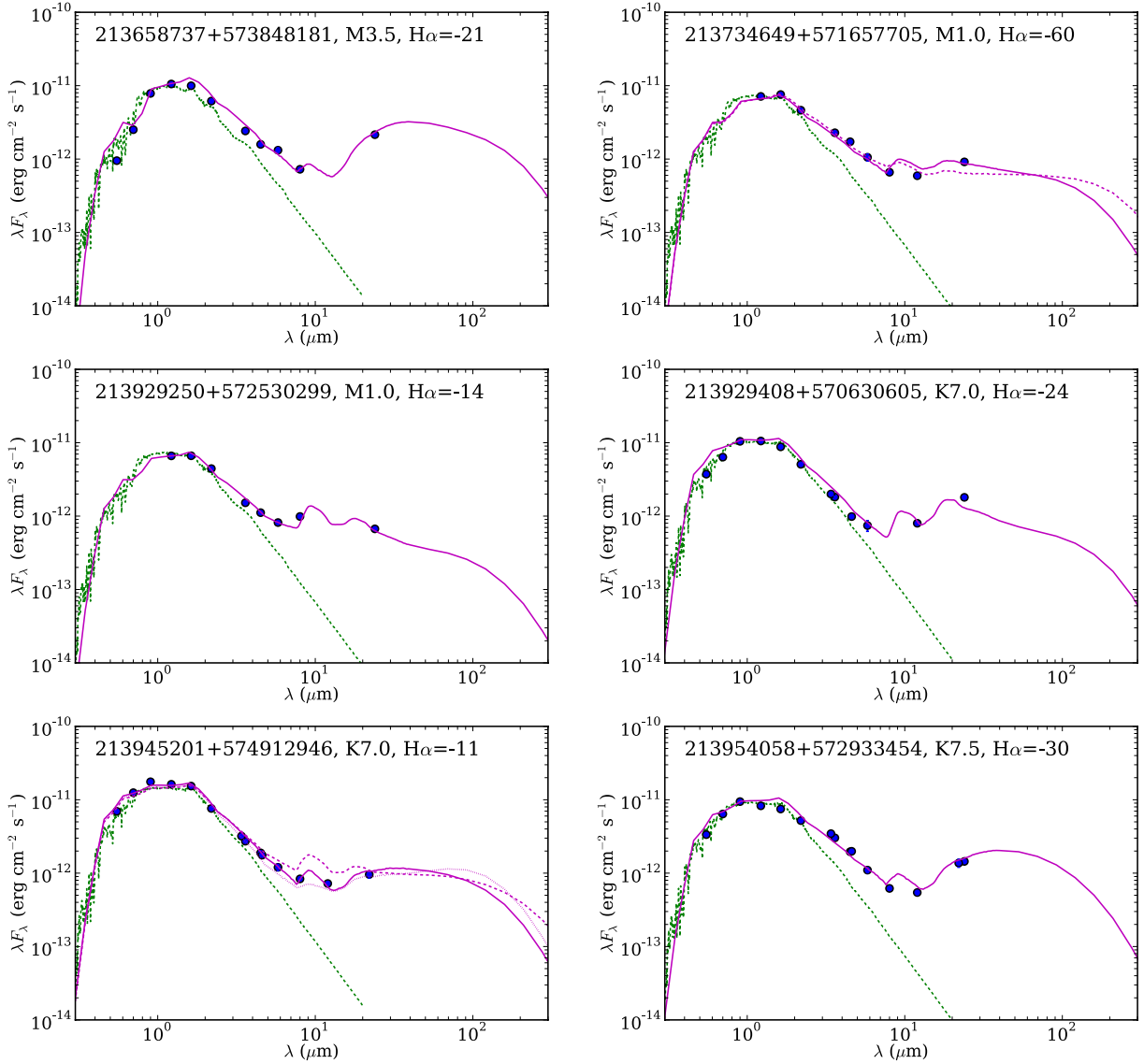


Fig. 10. Disk models for selected SEDs of pre-transitional disks (magenta lines). See Table 4 for information on the individual models. For comparison, the photosphere of a star with the same spectral type from the MARCS models (Gustafsson et al. 2008) is displayed. All datapoints have been extinction-corrected according to their individual values of A_V and assuming a standard extinction law (see Table A.1). Information about the $H\alpha$ EW (in \AA) is also displayed.

Among the 218 stars with disks (excluding Class I and uncertain objects), the full-disk objects are the most numerous, with a total of 111 stars (about 51% of the total). The least numerous are the pre-transitional disks (21 disks or nearly 10% of the total) and depleted disks (25 objects, about 11% of the total). The detection rate of PTD is low probably because of the lack of silicate feature observations. Our study of IRS spectra (SA11) suggests that the group of PTD is likely more numerous than estimated here from photometry alone. The group of dust-depleted objects has to be also regarded as a lower limit, since detection of low $24\ \mu\text{m}$ excesses among the latest-type stars are also compromised. Finally, transitional disks sum up to 61 objects, or about 28% of the sample. In total, objects with evidence for inside-out evolution (considering as such both transitional and pre-transitional disks) conform nearly 38% of the total sample, being a substantial fraction of the total population of disked objects. An important degree of dust evolution has thus occurred in Tr 37, also in agreement with the significantly low accretion

rates observed among cluster members (SA06b; Sicilia-Aguilar et al. 2010), suggestive of parallel dust and gas evolution in the disks.

Our current spectra do not allow us to estimate the accretion rates of the observed objects due to the uncertainty in the sky subtraction. However, considering as a typical value that of $3 \times 10^{-9} M_{\odot}/\text{yr}$ (Sicilia-Aguilar et al. 2010), and an age of 4 Myr, one would expect that the disks would have had a minimum disk mass of $0.012 M_{\odot}$. To reconcile this value with the typical disk masses observed, in general lower by at least a factor of few to one order of magnitude, strong grain growth needs to be taken into account. This is particularly important in case of the disks with very low dust masses and relatively strong $H\alpha$ emission (like 213751210+572436151), that would be about to lose their disks within less than 10^4 yr. If we do not include strong grain evolution or an anomalous gas to dust fraction, we would need to assume that are witnessing a very special moment of disk evolution in Tr 37, where a large fraction of disks is expected to

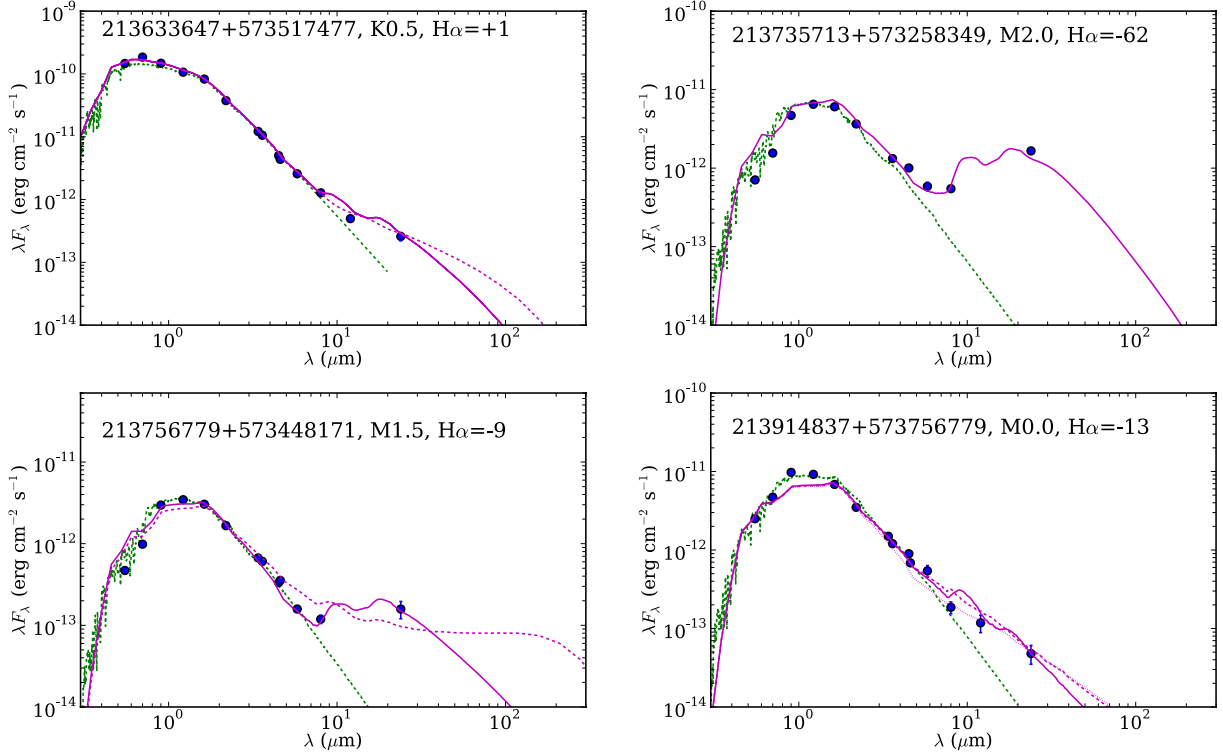


Fig. 11. Disk models for selected SEDs of transitional disks (magenta lines). See Table 4 for information on the individual models. For comparison, the photosphere of a star with the same spectral type from the MARCS models (Gustafsson et al. 2008) is displayed. All datapoints have been extinction-corrected according to their individual values of A_V and assuming a standard extinction law (see Table A.1). Information about the $H\alpha$ EW (in Å) is also displayed.

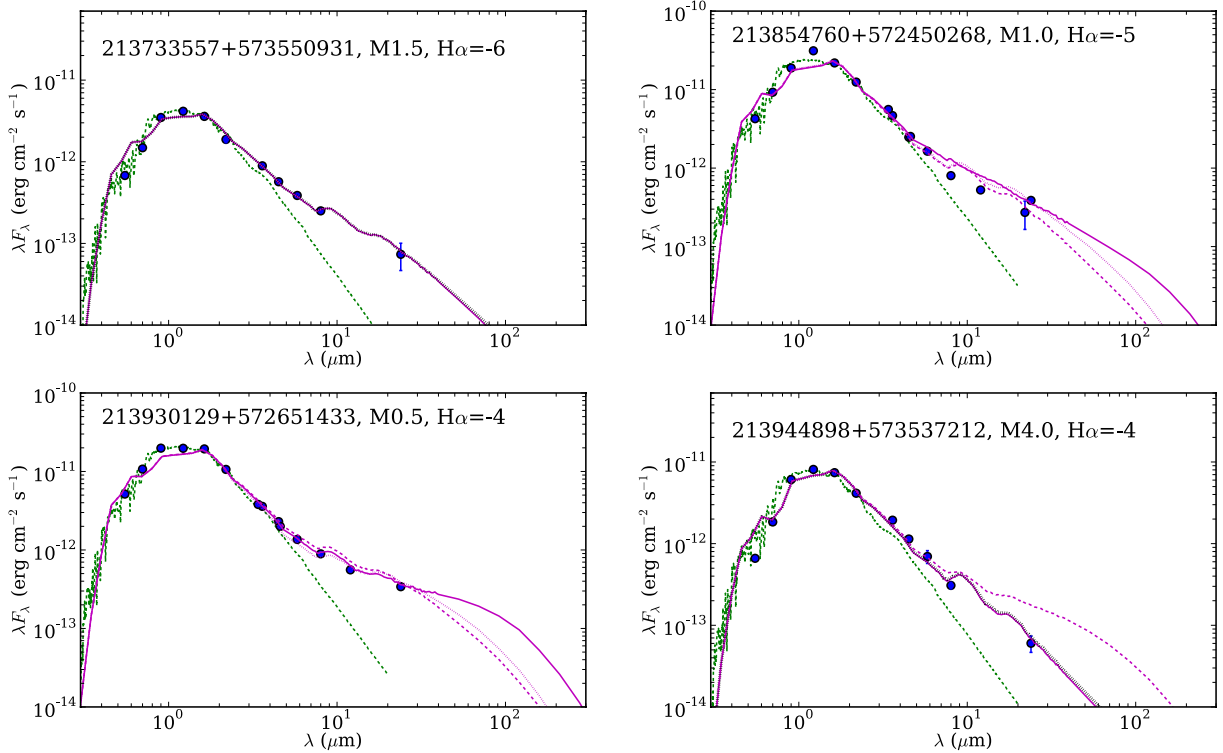


Fig. 12. Disk models for selected SEDs of dust-depleted disks (magenta lines). See Table 4 for information on the individual models. For comparison, the photosphere of a star with the same spectral type from the MARCS models (Gustafsson et al. 2008) is displayed. All datapoints have been extinction-corrected according to their individual values of A_V and assuming a standard extinction law (see Table A.1). Information about the $H\alpha$ EW (in Å) is also displayed.

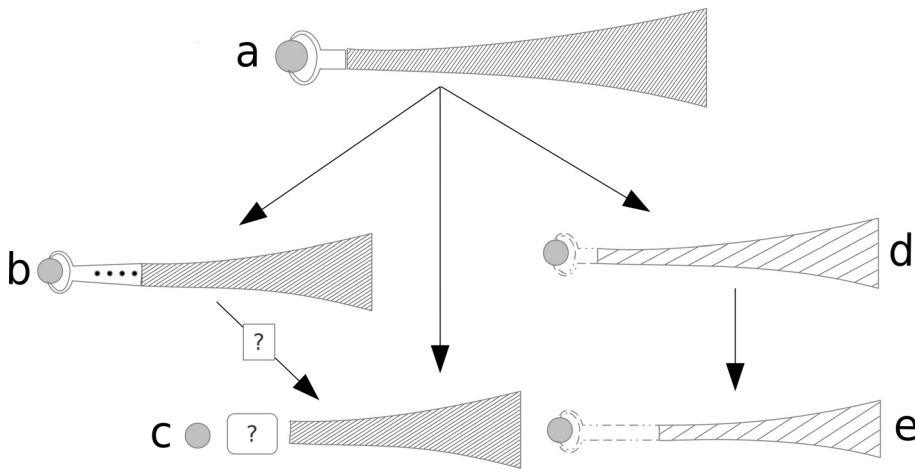


Fig. 13. Sketch of the different evolutionary paths discussed in the text. The full, accreting disk is represented by the sketch “a”. Such a disk can evolve in (at least) 3 different ways: suffering strong grain growth and ending up as an accreting TD (b), suffering other inner-disk removal processes (e.g. photoevaporation, removal by massive companions of stellar or planetary origin) to result in a nonaccreting TD (c), or experiencing small-dust removal at all radii (due for instance to generalized grain growth) and resulting in a small-dust depleted disk, typically with reduced accretion (d). While accreting TD may later on transform into nonaccreting TD or even dust-depleted TD (e), dust-depleted disks would not go through a typical TD stage (b, c) even if they later on also disperse from the inside-out (e). The list of evolved structures is not supposed to be complete, and the final outcome of each evolutionary path (e.g. star with planetary system) is not constrained with our present data.

disperse within the next $\sim 10^5$ years, which is highly unlikely from the statistical point of view and considering the age spread among Tr 37 members. Dust evolution (and thus a higher disk mass than expected) would be the only way to ensure that formation of giant planets is still possible among Tr 37 disks, if it has not occurred yet.

We also find evidence that not all disks evolve along the same path. Some TD have very large $24\ \mu\text{m}$ excesses, while others appear to be also dust-depleted, a sign that inner holes can appear both in massive, small-grain-rich, disks and in disks that are substantially depleted of small dust grains. Other disks are depleted of small dust grains but still have near-IR excesses, suggesting that small-dust depletion alone does not trigger the immediate opening of a hole in the disk. Moreover, although dust-depleted disks will also probably suffer inside-out evolution later on and enter the class of dust-depleted TD, they will not go through the “classical” TD phase (with no near-IR excess followed by a sharp increase at mid-IR wavelengths and a strong $24\ \mu\text{m}$ excess), given that they do not have enough mass nor vertical scale height. This would need to be considered when estimating the lifetime of “classical” TD. The diversity of objects is a sign of the different disk dispersal processes at work in a cluster as old as Tr 37 (~ 4 Myr for the central population). The differences observed between the accretion behavior of full-disks and TD/dust-depleted objects discussed in Sect. 4.1 suggests that gas accretion and dust evolution evolve in a parallel way. However, the fact that about 50% of TD are consistent with no accretion, while this is exceptionally rare among normal full-disks, is also a sign that not all disks with similar SEDs correspond to physically similar objects, confirming our previous results (Sicilia-Aguilar et al. 2010, SA11).

The stars in Tr 37 reveal several paths of disk evolution (see a sketch of disk types in Fig. 13). In general, evolution occurs from the inside-out, but the time scale when an inner hole develops in a disk appears to be different: in some cases, substantial dust depletion, settling, or both, occur without the disk developing an inner hole, while in some other cases, disks develop an inner hole while still being massive and very flared. To open a hole by photoevaporation (e.g. Clarke et al. 2001; Alexander et al. 2006; Gorti et al. 2009), the accretion rate or viscous transport through the disk needs to drop below a certain

level first. Therefore, in general objects with no significant accretion, low dust mass, and inner holes are good candidates to photoevaporation-related holes or to very massive companions that can block accretion. Nevertheless, very massive disks would also be less likely to disperse via photoevaporation until their mass and accretion rate have decreased sufficiently to prevent refilling of the inner hole by viscous evolution. This would make it more likely that their holes are related to other processes, like stellar companions or planet formation. Objects with transitional and dust-depleted disks that still have significant accretion are good candidates to suffer strong grain growth (maybe combined with settling), which would affect the IR excess but not the accretion rate, or very low-mass companions, that would not block the flow of gas through the gap. In the case of PTD, the differences in dust properties (especially, grain size) observed between the inner and the outer disk could be due to dust filtering in a planet-formation scenario (Rice et al. 2006), as we had also previously suggested in SA11. Recent spatially resolved observations show that the possibility of dust filtering/dust trapping in certain parts of the disk is a real one, and that gas flow across gaps appears to occur (Van der Marel et al. 2013; Casassus et al. 2013). More data, in particular, silicate feature observations, and ideally also spatially resolved observations, would be needed to better define the class of PTD.

We also explored the dependency of SED shape and disk structure with the spectral type/stellar mass. Figure 14 shows a plot of the median SED for the K-type and M-type objects with disks, scaled in both cases to the flux in band H and corrected by the individual extinction values of the objects. The plot includes the results of all the known members with well-defined IR excesses, excluding those with anomalous SEDs and/or photometric problems. This sums up to 76 K-type stars and 109 M-type stars. Although M-type stars have systematically lower IR excesses over the photosphere and the upper quartile for M-type stars hardly reaches the mean values for the K-type objects, the difference is not as dramatic as observed in the Coronet cluster (Currie & Sicilia-Aguilar 2011). The $24\ \mu\text{m}$ data in Tr 37 are not complete, so we expect to miss a substantial part of the objects with low $24\ \mu\text{m}$ excesses, especially among the fainter M-type stars. Nevertheless, the most striking result in the young (1–2 Myr) Coronet cluster is not the presence of disks

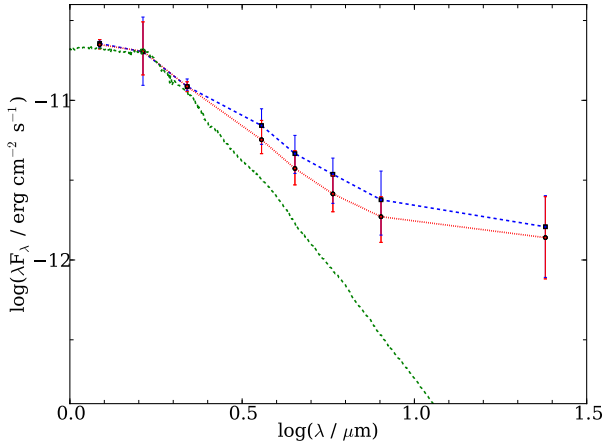


Fig. 14. Median SED for the objects with disks for spectral type K (blue dashed line) and M (red dotted line), with quartiles at each wavelength.

with very low masses, but the absence of massive disks among the M-type stars, which is not the case in Tr 37. The analysis of the $H\alpha$ EW in the different spectral type classes in Tr 37 also suggest that K- and M-type stars in Tr 37 are more similar in terms of accretion and disk properties than their counterparts in the Coronet cluster. Disks around M-type stars in Tr 37 are apparently *less evolved* than in the Coronet cluster, although we would expect the opposite from their ages, a signature that time evolution alone cannot explain the observed disk properties in Tr 37 and the Coronet cluster.

Besides age, the main differences between the Coronet cluster and Tr 37 are the number of members and the stellar density. In the Coronet cluster, we find about 50 stars (including resolved multiple systems) within a radius of about 0.15 pc (Sicilia-Aguilar et al. 2013). The membership count is probably close to complete for spectral types between B9 and M6, considering that the cluster has been observed in the optical, X ray, IR, and submillimeter (e.g. López-Martí et al. 2005, 2010; Groppi et al. 2004, 2007; Peterson et al. 2011; Sicilia-Aguilar et al. 2008, 2011a). Taking into account only the number of stars and not their mass, we arrive to a stellar density of about 3000 stars/pc³. In Tr 37, if we take a cluster radius of 5 pc, we count about 360 stars with spectral types O6 to M6, including both disked and diskless objects. If we account for a similar number of stars without disks that we may have missed in our surveys, and allow for a binarity rate of 50%, we arrive to about 1000 stars in total, resulting in a density of 2 stars/pc³. Even if our member number estimates are wrong by a factor of few, the density difference between both regions would still be close to 3 orders of magnitude.

The outskirts of the cluster may be less dense than the cluster center (e.g. Barentsen et al. 2011), but the difference in stellar density between the Coronet and Tr 37 would still be very large. Even if we consider that Tr 37 has suffered substantial expansion to arrive to its current stage (at a typical rate of 1 pc/Myr), an initial cluster size of 2 pc would only produce a density of 30 stars/pc³. Moreover, *Spitzer* observations (SA06a) and isochrone considerations (SA05; Getman et al. 2012) suggest that the population in the outskirts is most likely younger and formed in-situ, not by expansion of the original cluster. According to Sect. 7 of Getman et al. (2012) there are 235 (>60) stars down to 0.1 M_{\odot} near (inside) the IC 1396A globule, within the volume of roughly 75 pc³ (7 pc³). Assuming a binary rate of 50%, this gives 5 stars/pc³ (10 stars/pc³) near (inside) the

globule. This source density is still much lower than that of the Coronet cluster. The immediate result is that, while the early formation phases of stars in a compact, dense cluster like the Coronet would be heavily compromised by star-star interactions that could affect envelopes and disks, the environment in Tr 37 would have been much less interactive, allowing for larger envelopes and also larger disks masses. The initial disk structure may also pre-determine the evolutionary path that the disk will follow. Later on, other phenomena like the effect of the central O6 star may also contribute to disk dispersal in Tr 37 (e.g. Mercer et al. 2009).

4.4. The star-cloud interactions in Tr 37: mini-clusters and sequential star formation

Besides the fact that the O6 star HD 206267 shapes the large IC 1396A globule and other structures in the outskirts of Tr 37, our forbidden line images also reveal a smaller-scale interaction between some of the low-mass members and the remaining cloud. Figure 15 reveals a complex shocked structure in the surroundings of V390 Cep (21:36:50.72 +57:31:10.7, also known as MVA-60; Marschall & Van Altena 1987) and the K6 star 14–141 (Sicilia-Aguilar et al. 2004). The star 14–141 is known to show variable accretion and to be associated to variable forbidden line emission suggestive of time-variable shocks in the proximities of the star (Sicilia-Aguilar et al. 2010). In addition, the [S II] images reveal a large area emitting in forbidden lines, associated to the rim of the cloud in the proximity of 14–141. It is not possible to distinguish whether the shock is due to 14–141 or associated to more embedded objects within the cloud. There is a very embedded, reddened object that can be seen in the *Spitzer* images, although due to the variable background it is not possible to extract accurate photometric information from it.

There is also evidence of a small jet or shock on the other side of the bubble surrounding 14–141, with no object related to it. From its location, it could be related to V390 Cep, which is classified as a variable Ae star (despite its lack of IR excess at any of the *Spitzer* wavelengths). The shock emission would be located at about 13000 AU projected distance from V390 Cep. In addition, our Hectospec spectra reveal forbidden emission towards a few other stars (213744131+573331130, 213810759+574013683, 213942378+573348653, and 214059633+572210994; see Table A.5). All this suggest that even the low-mass stars in the cluster contribute to shaping the surrounding cloud, which could have an effect on local star formation.

We had already mentioned the age difference between the solar-type stars in the cluster center compared to the most embedded objects to the west of Tr 37, located within the IC 1396A globule (SA05; SA06a; Barentsen et al. 2011; Getman et al. 2012). In this spectroscopic survey, we took advantage of our previous knowledge of the cloud structure to obtain spectra of the objects associated with some smaller globules (of the order of 20''–40'', or approximately 0.1–0.2 pc at a distance of 870 pc; Contreras et al. 2002). The most remarkable structures contain 6 and 2 stars clearly associated with the extended IR emission, respectively, plus other surrounding objects that could be either associated or projected onto the nebula, forming what we call here “mini-clusters” (Fig. 16).

The larger globule or mini-cluster (Fig. 16, left) is remarkable because of the very strong $H\alpha$ emission of all its associated stars, which have very strong IR excesses as well. This small stellar group had been already noticed in the $H\alpha$ survey by Barentsen et al. (2011) and in the X-ray/IR study of

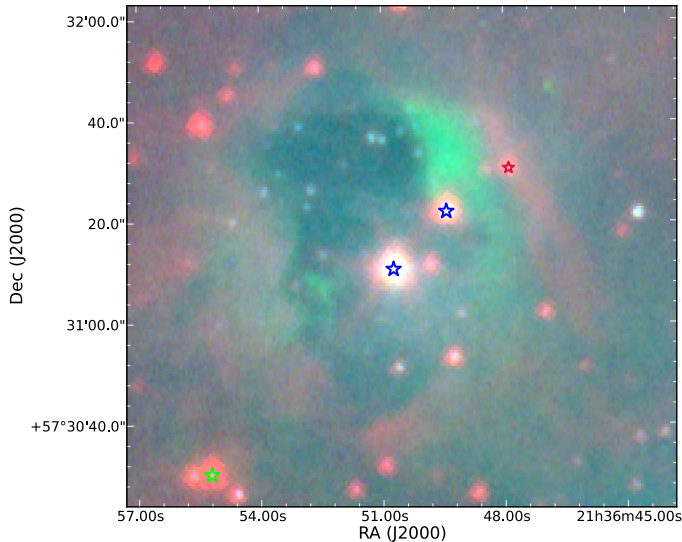


Fig. 15. Detail of the 3-color (IRAC1, [S II] combined at 6716 and 6730 Å, and *R* band as red, green, and blue, respectively) image of the IC 1396 A globule, zooming around V390 Cep (in the center of the clearing) and 14-141 (marked in blue). Embedded *Spitzer*-detected objects are marked as red stars.

Getman et al. (2012), Sect. 8.3.2. The region also host the binary B3+B5 star CCDM+5734, which was found to have a transitional disk with a large hole and evidence of small silicate dust (Sicilia-Aguilar et al. 2007). The second structure (Fig. 16, right) contains the star 213911452+572425205. This object appears as emerging from the cloud tip and shows a large IR excess and a large number of accretion-related emission lines in its spectrum. The globule also contains 213905519+572349596, a star without evidence of disk nor accretion. Although obtaining ages of these embedded objects is problematic, the extreme $H\alpha$ values and IR excesses of all of them (except 213905519+572349596) could indicate that the stars are younger than the general Tr 37 population, either related to triggered or sequential star formation within small surviving globules in the cluster, or maybe to structures in the younger outskirts of the cluster, seen in projection, or clumpy star formation.

5. Summary and conclusions

We performed a spectroscopic survey targeting the low-mass members of the 4 Myr-old cluster Tr 37. The spectra allowed us to identify a large number of new members and, together with our already available data (optical photometry, 2MASS, and IR *Spitzer* IRAC and MIPS data), to study the connection between accretion indicators and IR excesses from protoplanetary disks. From our study, Tr 37 emerges as a relatively evolved young cluster where its surviving disks display a variety of evolutionary signs. The results of this work are summarized below:

- The survey provided data on spectral types, accretion, and extinction for 205 cluster members and probable members, leading to the discovery of 78 new cluster members, and 64 probable members. Most of these members are M-type (M0–M5) stars with IR excesses typical of protoplanetary disks and accretion indicators.
- Gas accretion, detected via the $H\alpha$ EW, is strongly correlated with the presence of disks. A KS test including the new and the previously known members reveals a nominally 0 probability that both disked (with all types of disks) and

diskless objects are drawn from the same distribution. We also find significant differences between the accretion behavior of full-disks and disks with strong evidence of evolution (TD and dust-depleted disks). About half of the TD are consistent with no accretion (being similar to diskless stars), while the other half have $H\alpha$ values similar to full-disks. Dust-depleted disks, in particular those around M-type stars, also show significantly lower $H\alpha$ EW. This suggests that dust and gas evolve in a parallel way: objects with no evidence of dust evolution are very unlikely to have suffered accretion termination, while accretion termination (or very strong suppression of accretion) is common among transitional and dust-depleted disks. The difference in accretion behavior between dust depleted and full disks also suggests that objects with very low $24\ \mu\text{m}$ excesses are in a different evolutionary stage, although it is not possible to tell if this is caused by parallel dust and gas evolution, by strong dust settling after partial gas depletion, or by both.

- We find a tentative trend (limited by low number statistics) that accreting TD are more frequent among M-type stars than among GK-type stars, which could be either related to the larger holes in the disks around GK-type stars for the same IR excess, or indicate that accretion last longer in the TD around M-type stars. GK-type dust-depleted disks are generally accreting, in contrast with M-type dust-depleted disks, pointing to a faster termination of accretion in M-type stars after global dust evolution. Further observations of similar objects are required to confirm or reject these points.
- We used the RADMC radiative transfer code to model a sample of disks with different types of SEDs. Full-disks can be reproduced with simple models with different degrees of grain growth, vertical scale height, and disk masses. Transitional disks require an inner hole to account for the lack of near-IR excess, although the hole size (or the temperature of the inner disk rim) is highly dependent on the dust properties and vertical scale height. Pre-transitional disks models require a change in disk properties between the innermost and outer disk, although there is a high degree of degeneracy between location of the radius at which the properties change, dust distributions on both sides, and vertical scale heights. Dust-depleted disks with very low 8–24 μm fluxes and reduced near-IR excesses require substantial mass depletion, if we assume the disk is in hydrostatic equilibrium. Strong settling may contribute to low near-IR excess, but a dust mass in small (<20 μm) grains significantly lower than in full disks is still needed to account for the low mid-IR fluxes and the steep shape of the SED.
- Including all the Tr 37 population identified in this and in the previous study (over 200 objects with spectral types G, K, and M), we studied the prevalence of signs of inside-out evolution and dust depletion in the disks. More than 1/3 of the disks show signs of inside-out evolution (inner holes, or changes in disk properties between the inner and outermost disk). About 10% of the disks have significant dust depletion, resulting in very low mid-IR fluxes and typically low accretion rates. Nearly 20% of the disks with inner holes (TD) have also very low mid-IR excesses and are most likely dust depleted as well. Among full-disks, substantial evolution in the form of grain growth needs also to be assumed to obtain disk masses in the appropriate range for the accretion rates observed.
- The diversity of disks in Tr 37 suggests that not all disks follow the same evolutionary path: while inside-out evolution seems to be the rule, we find that some disks develop inner

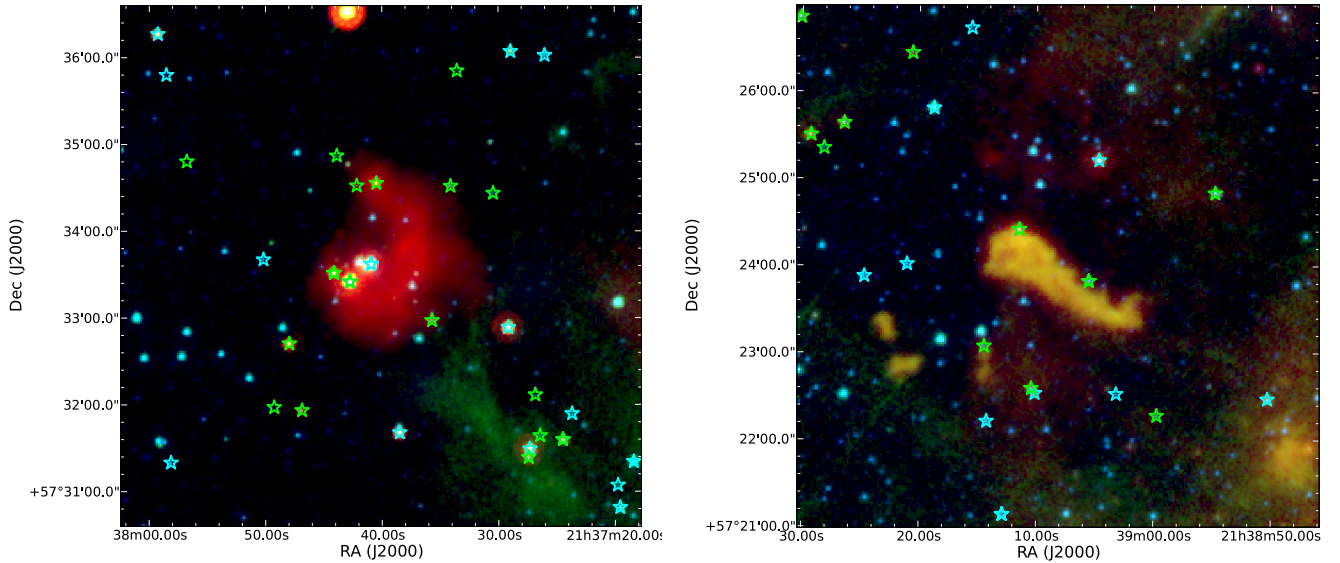


Fig. 16. Two 3-color (3.6, 8, 24 μm) image of the small globules or mini-clusters in Tr 37. Previously known members are marked as cyan stars, new members (from this work) are marked as green stars.

holes while keeping a relatively massive outer disk, while others lose a significant fraction of their small dust grains before their inner parts are cleared. This points to several effects contributing to disk dispersal.

- Our study of Tr 37 does not reveal the striking differences observed the young Coronet cluster, among K-type and M-type stars (Currie & Sicilia-Aguilar 2011). Non-accreting and depleted disks among M-type stars are not as frequent as in the Coronet, even though Tr 37 is substantially older. A possible explanation is the very different environment and, in particular, the stellar density in both regions. While recent studies suggest a density of the order of 3000 stars/pc³ in the sparse Coronet cluster, the density in Tr 37 is about 2–3 orders of magnitude lower. This suggests that the differences in disk properties observed between both regions could be related to very different environment and initial conditions, like early interactions. Frequent close interactions at a protostellar level could result in lower initial disk masses and a lack of massive disks among low-mass stars, which is what we observe in the Coronet cluster.
- Finally, we also studied the stellar content of several small globules in Tr 37, finding that some of them harbor mini-clusters with a few members. The stars within these mini-clusters show preferentially full-disks with strong IR excesses and strong emission lines. This suggests that the objects could be younger than the extended Tr 37 population, which could be indicative of very small-scale sequential (or clumpy) star formation in the region.

Acknowledgements. The authors are grateful to V. L. Afanasiev for conducting the SCORPIO observations, and V. V. Krushinsky and P. A. Boley for their help in the preparation of the observations with the 6 m Telescope of SAO RAS, to P. Berlind, N. Caldwell, and M. Calkins at the MMT observatory, and to M. Alises, F. Hoyo, and S. Pedraz at Calar Alto Observatory. We also thank C. Dullemond for his help with the RADMC code, and the anonymous referee for his/her careful comments that helped to clarify and organize this paper. Based on observations collected at the German-Spanish Astronomical Center, Calar Alto, jointly operated by the Max-Planck-Institut für Astronomie Heidelberg and the Instituto de Astrofísica de Andalucía (CSIC). We also thank Calar Alto Observatory for allocation of director’s discretionary time to this program. This work is based on observations made with the *Spitzer* Space Telescope, which is operated by the Jet Propulsion Laboratory, California Institute of Technology under a contract with NASA. This publication makes use of data products from the

Wide-field Infrared Survey Explorer, which is a joint project of the University of California, Los Angeles, and the Jet Propulsion Laboratory/California Institute of Technology, funded by the National Aeronautics and Space Administration. It also makes use of data products from the Two Micron All Sky Survey, which is a joint project of the University of Massachusetts and the Infrared Processing and Analysis Center/California Institute of Technology, funded by the National Aeronautics and Space Administration and the National Science Foundation. A.S.A. acknowledges support of the Spanish MICINN/MINECO “Ramón y Cajal” program, grant number RYC-2010-06164, and the action “Proyectos de Investigación fundamental no orientada”, grant number AYA2012-35008. MF is also supported by AYA2012-35008.

References

- Afanasiev, V. L., & Moiseev, A. V. 2005, *PaZh*, 31, 214
Alexander, R. D., & Armitage, P. J. 2009, *ApJ*, 704, 989
Alexander, R., Clarke, C., & Pringle, J. 2006, *MNRAS*, 369, 229
Apai, D., Pascucci, I., Bouwman, J., et al. 2005, *Sci*, 310, 834
Appenzeller, I., Jankovics, I., & Jetter, R. 1986, *A&ASS*, 64, 65
Arzoumanian, D., André, P., Didelon, P., et al. 2011, *A&A*, 529, L6
Barentsen, G., Vink, J. S., Drew, J. E., et al. 2011, *MNRAS*, 415, 103
Bate, M. R. 2012, *MNRAS*, 419, 3115
Bate, M., & Bonnell, I. A. 2005, *MNRAS*, 356, 1201
Bessell, M. S., & Brett, J. M. 1988, *PASP*, 100, 113
Bouwman, J., Lawson, W. A., Dominik, C., et al. 2006, *ApJ*, 653, 57
Cardelli, J., Clayton, G., & Mathis, J. 1989, *ApJ*, 345, 245
Casassus, S., van der Plas, G., Sebastian Perez, D., et al. 2013, *Nature*, 493, 191
Clarke, C., & Pringle, J. 2006, *MNRAS*, 370, L10
Clarke, C., Gendrin, A., & Sotomayor, M. 2001, *MNRAS*, 328, 485
Cieza, L., Padgett, D. L., Stapelfeldt, K. R., et al. 2007, *ApJ*, 667, 308
Contreras, M. E., Sicilia-Aguilar, A., Muzerolle, J., et al. 2002, *AJ*, 124, 1585
Currie, T., & Sicilia-Aguilar, A. 2011, *ApJ*, 732, 24
Currie, T., Lada, C. J., Plavchan, P., et al. 2009, *ApJ*, 698, 1
Cutri R. M., Skrutskie, M. F., van Dyk, S., et al. 2003, *yCat.2246, 0C*, *VizieR On-line Data Catalog: II/246*
Dorschner, J., Begemann, B., Henning, T., Jäger, C., & Mutschke, H. 1995, *A&A*, 300, 503
Dullemond, C., & Dominik, C. 2004, *A&A*, 417, 159
Dullemond, C., Natta, A., & Testi, L. 2006, *ApJ*, 645, L69
Espaillat, C., D’Alessio, P., Hernández, J., et al. 2010, *ApJ*, 717, 441
Espaillat, C., Ingleby, L., Hernández, J., et al. 2012, *ApJ*, 747, 103
Fang, M., van Boekel, R., Wang, W., et al. 2009, *A&A*, 504, 461
Fang, M., van Boekel, R., Bouwman, J., et al. 2013a, *A&A*, 549, A15
Fang, M., Kim, J. S., van Boekel, R., et al. 2013b, *ApJS*, 207, 5
Fedele, D., van den Ancker, M. E., Henning, T., Jayawardhana, R., & Oliveira, J. M. 2010, *A&A*, 510, A72
Fernie, J. 1983, *PASP*, 95, 782
Gatti, T., Natta, A., Randich, S., Testi, L., & Sacco, G. 2008, *A&A*, 481, 423

- Getman, K. V., Feigelson, E. D., Sicilia-Aguilar, A., et al. 2012, MNRAS, 426, 2917
- Groppi, Kulesa, C., Walker, C., et al. 2004, ApJ, 612, 946
- Groppi, C. E., Hunter, T. R., Blundell, R., & Sandell, G. 2007, ApJ, 670, 489
- Gullbring, E., Hartmann, L., Briceño, C., Calvet, N. 1998, ApJ, 492, 323
- Gustafsson, B., Edvardsson, B., Eriksson, K., et al. 2008, A&A, 486, 951
- Hacar, A., Tafalla, M., Kauffmann, J., & Kovács, A. 2013, A&A, 554, A55
- Haisch, K., Lada, E., & Lada, C. 2001, ApJ, 553, 153
- Hamann, F. 1994, ApJS, 93, 485
- Hammann, F., & Persson, S. E. 1992, ApJS, 82, 247
- Hartmann, L. 2003, ApJ, 585, 398
- Hartmann, L., D'Alessio, P., Calvet, N., & Muzerolle, J. 2006, ApJ, 648, 484
- Harvey, P. M., Jaffe, D. T., Allers, K., & Liu, M. 2010, ApJ, 720, 1374
- Harvey, P. M., Henning, T., Ménard, F., et al. 2012a, ApJ, 744, L1
- Harvey, P. M., Henning, T., Liu, Y., et al. 2012b, ApJ, 755, 67
- Herczeg, G. J., & Hillenbrand, L. A. 2008, ApJ, 681, 594
- Hernández, J., Hartmann, L., Megeath, S. T., et al. 2007, ApJ, 662, 1067
- Hernández, J., Hartmann, L., Calvet, N., et al. 2008, ApJ, 686, 1195
- Jäger, C., Mutschke, H., Begeman, B., Dorschner, J., & Henning, Th. 1994, A&A, 292, 641
- Jayawardhana, R., Mohanty, S., Basri, G. 2005, Mem. S. A. It. 76, 295
- Jeffries, R. D., Naylor, T., Walter, F. M., Pozzo, M. P., & Devey, C. R. 2009, MNRAS, 393, 538
- Kenyon, S. J., & Hartmann, L. 1995, ApJS, 101, 117
- Kessler-Silacci, J., Dullemond, C. P., Augereau, J.-C., et al. 2007, ApJ, 659, 680
- Kirkpatrick, J. D., Henry, T. J., & Simons, D. A. 1995, AJ, 109, 797
- Klein, R., Apai, D., Pascucci, I., Henning, Th., & Waters, L. 2003, ApJ, 593, 57
- Lawson, W., Lyo, A., & Muzerolle, J. 2004, MNRAS, 329, 29
- López-Martí, B., Eislöffel, J., & Mundt, R. 2005, A&A, 444, 175
- López Martí, B., Spezzi, L., Merín, B., et al. 2010, A&A, 515, A31
- Martín, E., Rebolo, R., & Zapatero-Osorio, M. R. 1996, ApJ, 469, 706
- Marschall, L. A., & van Altena, W. F. 1987, AJ, 94, 71
- Mercer, E. P., Miller, J. M., Calvet, N., et al. 2009, AJ, 138, 7
- Merín, B., Brown, J. M., Oliveira, I., et al. 2010, ApJ, 718, 1200
- Meyer, M. R., Calvet, N., & Hillenbrand, L. A. 1997, AJ, 114, 288
- Mohanty, S., Jayawardhana, R., Natta, A., et al. 2004, ApJ, 609, L33
- Morrow, A. L., Luhman, K. L., Espaillat, C., et al. 2008, ApJ, 676, 143
- Muench, A., Alves, J., Lada, Ch., & Lada, E. 2001, ApJ, 558, 51
- Muzerolle, J., Allen, L. E., Megeath, S. T., Hernández, J., & Gutermuth, R. A. 2010, ApJ, 708, 1107
- Najita, J., Strom, S., & Muzerolle, J. 2007, MNRAS, 368, 379
- Natta, A., Testi, L., Neri, R., Schepherd, D., & Wilner, D. 2004, A&A, 416, 179
- Natta, A., Testi, L., Randich, S., & Muzerolle, J. 2005, Mem. S. A. It., 76, 343
- Oliveira, I., Merín, B., Pontoppidan, K. M., & van Dishoeck, E. F. 2013, ApJ, 762, 128
- Pascucci, I., Apai, D., Luhman, K., et al. 2009, ApJ, 696, 143
- Patel, N. A., Goldsmith, P. F., Snell, R. L., Hezel, T., & Xie, T. 1995, ApJ, 447, 721
- Patel, N. A., Goldsmith, P. F., Heyer, M. H., & Snell, R. L. 1998, ApJ, 507, 241
- Peterson, D. E., Caratti o Garatti, A., Bourke, T. L., et al. 2011, ApJSS, 194, 43
- Platais, I., Kozhurina-Platais, V., & van Leeuwen, F. 1998, AJ, 116, 2423
- Rice, W., Armitage, P., Wood, K., & Lodato, G. 2006, MNRAS, 373, 1619
- Riddick, F. C., Roche, P. F., & Lucas, P. W. 2007, MNRAS, 381, 1067
- Schol, A., & Jayawardhana, R. 2008, ApJ, 672, 49
- Schol, A., Jayawardhana, R., Wood, K., et al. 2007, ApJ, 660, 1517
- Sicilia-Aguilar, A., Hartmann, L., Briceño, C., Muzerolle, J., & Calvet, N. 2004, AJ, 128, 805 (SA04)
- Sicilia-Aguilar, A., Hartmann, L., Hernández, J., Briceño, C., & Calvet, N. 2005, AJ, 130, 188 (SA05)
- Sicilia-Aguilar, A., Hartmann, L., Calvet, N., et al. 2006a, ApJ, 638, 897 (SA06a)
- Sicilia-Aguilar, A., Hartmann, L., Fürész, G., et al. 2006b, AJ, 132, 2135 (SA06b)
- Sicilia-Aguilar, A., Hartmann, L., Watson, D., et al. 2007, ApJ, 659, 1637
- Sicilia-Aguilar, A., Henning, Th., Juhász, A., et al. 2008, ApJ, 687, 1145
- Sicilia-Aguilar, A., Bouwman, J., Juhász, A., et al. 2009, ApJ, 701, 1188
- Sicilia-Aguilar, A., Henning, Th., & Hartmann, L. 2010, ApJ, 710, 597
- Sicilia-Aguilar, A., Henning, T., Kainulainen, J., & Roccatagliata, V. 2011a, ApJ, 736, 137
- Sicilia-Aguilar, A., Henning, T., Dullemond, C. P., et al. 2011b, ApJ, 742, 39 (SA11)
- Sicilia-Aguilar, A., Henning, T., Linz, H., et al. 2013, A&A, 551, A34
- Siess, L., Dufour, E., & Forestini, M. 2000, A&A, 358, 593
- van der Marel, N., van Dishoeck, E. F., Bruderer, S., et al. 2013, Science, 340, 1199
- White, R., & Basri, G. 2003, ApJ, 582, 1109
- Whitworth, A., & Zinnecker, H. 2004, A&A 427, 299
- Wright, E. L., Eisenhardt, P. R. M., Mainzer, A. K., et al. 2010, AJ, 140, 1868

Appendix A: Complete data tables of observed objects, their classification, and the photometry of members and probable members

The following tables contain the full information (object type and membership) of the objects observed with Hectospec/MMT (Table A.1), followed by the photometry data on members and probable members (Tables A.2 and A.3).

Table A.1. Observations and spectroscopic information.

Spect. ID	H α EW (Å)	Li EW (Å)	Sp. Type	A $_V$ (mag)	Disk?	Campaign	Member?	Comments
213539203+573021561	Abs.	–	X	–	X	2009-MMT	N	
213541592+573127753	Abs.	–	X	–	X	2010-MMT	N	
213542993+573337049	–16	–	M4.0	1.1 \pm 0.6	Y	2009-MMT	Y ⁴	
213554323+573443434	–8	–	Late	–	N	2009-MMT	N	
213555607+573003406	Abs.	N	G9.0	6.4 \pm 1.9	N	2010-MMT	N	
213601910+573430689	–1	–	K3.0	3.1 \pm 0.0	Y	2009-MMT	X	
213602343+573326502	Abs.	–	G9.0	2.8 \pm 0.2	Y	2009-MMT	N	
213602762+572834046	Abs.	–	X	–	N	2009-MMT	N	
213603888+572712198	Abs.	–	X	–	pN	2010-MMT	N	
213606037+573139138	–0.1	–	K1.5	3.6 \pm 0.1	Y	2009-MMT	N	
213607980+572637096	–11:	–	E-Class I	–	Y	2010-MMT	Y	
213610280+573249821	Abs.	–	K1.5	4.1 \pm 0.0	P	2009-MMT	N	
213611098+572801471	Abs.	–	K0.0	4.6 \pm 0.0	P	2009-MMT	N	
213615231+572958174	Abs.	N	K0.0	4.6 \pm 0.0	pN	2010-MMT	N	
213617003+572639925	–23	–	M3.5	0.8 \pm 0.5	N	2009-MMT	N	
213617593+572510785	Abs.	–	X	–	N	2009-MMT	N	
213617600+572353249	Abs.	–	K1.5	2.7 \pm 0.2	N	2009-MMT	N	
213618699+573626870	–4	0.3	M3.5	0.9 \pm 0.3	N	2009-MMT	Y	
213618850+572649552	–1	–	K1.0	2.8 \pm 0.2	P	2009-MMT	N	
213619969+573527805	–6	–	M4.5	1.3 \pm 0.8	N	2009-MMT	Y	
213620628+572839896	Abs.	–	X	–	pN	2010-MMT	X	
213622159+572327898	–12	–	M3.5	1.1 \pm 0.6	N(24)	2009-MMT	pN ⁴	Neb.
213622379+573141225	–9	0.1:	M3.0	3.3 \pm 0.9	pN	2010-MMT	Y	
213624769+572244914	Abs.	–	K1.0	3.4 \pm 0.1	N	2009-MMT	N	
213625078+572750265	–80	–	M4.0	1.2 \pm 0.6	Y	2009-MMT	Y ^{1, 2}	21362507.5727502
213626039+573327463	Abs.	–	K1.0	3.7 \pm 0.1	N	2009-MMT	N	
213626897+573304351	–21	–	M0.0	3.6 \pm 0.5	pN	2010-MMT	Y ⁴	Neb., Nobj.
213627742+573202223	Abs.	N	K3.0	5.9 \pm 1.8	pN	2010-MMT	N	
213633647+573517477	Abs.	–	K0.5	3.0 \pm 0.2	Y(24)	2009-MMT	Y	Var.?, oVVI
213634910+572612281	–5	pN	M1.0	1.7 \pm 0.6	pN(8)	2010-MMT	pN	
213635322+572622430	Abs.	–	K2.5	3.9 \pm 1.0	N	2009-MMT	N	
213636558+573559377	Abs.	–	K1.0	3.0 \pm 0.2	N	2009-MMT	N	
213636909+573132683	–20	–	K7.0	3.3 \pm 0.2	Y	2009-MMT	Y ⁴	
213637760+572458219	0	–	K1.0	3.5 \pm 0.2	N	2009-MMT	N	
213638543+573641056	–2	–	M3.0	0.4 \pm 0.5	N	2009-MMT	N	
213639147+572953326	–3	0.2	G9.0	5.3 \pm 0.4	Y	2009-MMT	Y ⁴	oVVI, Earlier?
213641152+573702713	–7	0.3	M1.5	2.0 \pm 0.7	N	2010-MMT	Y ⁴	
213641358+572204113	–11	0.1:	M2.0	2.0 \pm 1.0	N	2010-MMT	P	
213642470+572523186	–27	–	M3.5	1.4 \pm 0.7	Y	2009-MMT	Y ³	
213643679+572331935	Abs.	N	K1.5	5.5 \pm 1.7	pN	2010-MMT	N	
"	Abs.	N	K1.5	5.5 \pm 1.7	pN	2010-MMT	N	
213643940+571838724	0	–	G7.0	6.6 \pm 0.6	P	2009-MMT	N	
213647421+571942074	Abs.	–	K0.0	3.0 \pm 0.2	N	2009-MMT	N	
213648190+573402084	–2	–	M1.5	1.4 \pm 0.2	N	2009-MMT	Y ⁴	

Notes. The full table is available at the CDS. This table lists all observed objects, their Li and H α EW, and membership criteria. The objects IDs are based on the spectrograph (optical) coordinates. If H α appears in absorption, we label it as “Abs.” in the corresponding column. If Lithium absorption can be excluded for EW larger than 0.1, we label it as “N” in the corresponding column. Membership and presence of disks are marked as “Y” (yes), “N” (no), “P” (probable), and “pN” (probably not). In case the disk excess was observed only at one wavelength, we label it (e.g. P(24) indicates that the object has probably an excess, but only at 24 μ m). Undetermined values of the spectral type, uncertain membership, and uncertain IR fluxes are marked by “X”, objects with spectral types earlier than G are marked with “E”. The errors in the spectral type are of 0.5 subtypes for objects K5 or later, 1 subtype for early K stars, and 2–3 subtypes for G-type objects. The best spectral types (in case of multiple values due to different observations with different S/N) are marked with ^(b). Objects previously identified by Sicilia-Aguilar et al. (2005, 2006a,b) are marked with ⁽¹⁾ (and their previous names are given in the comments), those identified by Barentsen et al. (2011) are marked with ⁽²⁾, those in common with Morales-Calderón et al. (2009) are marked with ⁽³⁾, objects with X-ray counterparts in Getman et al. (2012) are marked with ⁽⁴⁾, and further IR-excess sources in the same paper are marked with ⁽⁵⁾. In the comments field, we mention if there is any problem due to IR nebular emission (Neb.), nearby objects (Nobj.), if the SED suggest that the object is variable (Var.), if the object appears older than 10 Myr in the V vs. V – I diagram (oVVI), or any other observation regarding the star/disk.

Table A.2. Optical and 2MASS data for confirmed members and probable members.

Spect. ID	V (mag)	R_J (mag)	I_J (mag)	2MASS ID	J (mag)	H (mag)	K (mag)
213542993+573337049	19.476 ± 0.011	17.613 ± 0.030	15.506 ± 0.002	21354299+5733370	14.302 ± 0.037	13.439 ± 0.033	13.075 ± 0.036
213607980+572637096	–	–	–	21360798+5726371	18.366:	17.484:	14.507 ± 0.088
213618699+573626870	19.516 ± 0.011	17.693 ± 0.030	15.870 ± 0.003	21361870+5736268	14.707 ± 0.046	13.911 ± 0.056	13.600:
213619969+573527805	21.154 ± 0.036	19.230 ± 0.032	16.871 ± 0.004	21361996+5735278	15.721 ± 0.065	15.084 ± 0.089	14.724 ± 0.089
213622159+572327898	19.269 ± 0.013	17.468 ± 0.023	15.416 ± 0.002	21362216+5723278	14.263 ± 0.044	13.496 ± 0.050	13.173 ± 0.039
213622379+573141225	21.277 ± 0.039	19.006 ± 0.031	16.251 ± 0.003	21362238+5731412	14.567 ± 0.036	13.792 ± 0.033	13.404 ± 0.037
213625078+572750265	20.435 ± 0.020	18.558 ± 0.024	16.399 ± 0.004	21362507+5727502	14.952 ± 0.044	14.031 ± 0.048	13.518 ± 0.040
213626897+573304351	20.963 ± 0.035	18.868 ± 0.031	16.709 ± 0.004	21362690+5733043	15.217 ± 0.055	14.158:	13.869:
213633647+573517477	15.826 ± 0.002	14.359 ± 0.030	13.236 ± 0.003	21363365+5735174	12.242 ± 0.024	11.458 ± 0.028	11.254 ± 0.023
213636909+573132683	19.424 ± 0.011	17.422 ± 0.030	15.828 ± 0.003	21363691+5731326	13.754 ± 0.031	12.631 ± 0.037	12.021 ± 0.026
213639147+572953326	18.040 ± 0.007	16.171 ± 0.022	14.129 ± 0.002	21363915+5729533	11.924 ± 0.021	10.422 ± 0.028	9.392 ± 0.021
213641152+573702713	20.024 ± 0.014	18.192 ± 0.030	16.175 ± 0.003	21364115+5737027	14.880 ± 0.044	14.132 ± 0.052	13.866 ± 0.056
213641358+572204113	20.596 ± 0.021	18.769 ± 0.024	16.515 ± 0.004	21364135+5722041	15.220 ± 0.067	14.613 ± 0.076	14.053 ± 0.059
213642470+572523186	19.997 ± 0.016	18.137 ± 0.023	15.958 ± 0.004	21364247+5725231	14.806 ± 0.043	14.089 ± 0.047	13.758 ± 0.049
213648190+573402084	19.159 ± 0.011	17.403 ± 0.030	15.819 ± 0.003	21364819+5734020	14.796 ± 0.043	13.989 ± 0.053	13.785 ± 0.047
213653210+572052112	20.084 ± 0.016	18.404 ± 0.023	16.521 ± 0.004	21365320+5720521	15.459 ± 0.056	14.806 ± 0.064	14.437 ± 0.073
213655201+573030103	21.367 ± 0.046	19.216 ± 0.032	17.013 ± 0.005	21365520+5730301	14.714 ± 0.078	12.665 ± 0.063	11.382 ± 0.034
213655283+572551668	17.220 ± 0.004	15.757 ± 0.022	14.678 ± 0.002	21365527+5725516	13.592 ± 0.030	12.812:	12.613:

Notes. The full table is available at the CDS. ^(a) Anomalous optical colors. ^(b) Near HD 206267. ^(c) Near 21–840, likely contaminated. ^(d) Near bright star, probably contaminated.

Table A.3. *Spitzer* IRAC and MIPS data for confirmed members and probable members.

Spect. ID	IRAC-1 (μ Jy)	IRAC-2 (μ Jy)	IRAC-3 (μ Jy)	IRAC-4 (μ Jy)	MIPS-1 (μ Jy)	SED	Comments
213542993+573337049	2683 ± 72	1982 ± 57	1808 ± 222	1211 ± 86	881 ± 157	Dep.	
213607980+572637096	19 571 ± 94	39 189 ± 78	103 489 ± 512	–	1 159 200 ± 6406	Class I	
213618699+573626870	1251 ± 53	835 ± 53	708 ± 197	146 ± 43	–	ND	
213619969+573527805	522 ± 3	343 ± 3	257 ± 15	163 ± 48	–	ND	
213622159+572327898	2220 ± 53	1434 ± 58	1244 ± 273	–	–	Neb. contamination	
213622379+573141225	1669 ± 43	1066 ± 55	1305 ± 196	1984 ± 230	–	ND	
213625078+572750265	3060 ± 58	3013 ± 61	3021 ± 224	4872 ± 26	9196 ± 103	Full	
213626897+573304351	1392 ± 54	750 ± 54	–	–	–	ND	Neb.
213633647+573517477	10 624 ± 79	6568 ± 51	4339 ± 221	2982 ± 72	1800 ± 310	TD/Dep.	Var.?
213636909+573132683	10 712 ± 33	10 062 ± 77	10 814 ± 257	15 797 ± 95	13 900 ± 3802	Full	
213639147+572953326	156 347 ± 511	–	155 812 ± 641	–	150 577 ± 2912	Full	
213641152+573702713	1045 ± 50	717 ± 54	488 ± 220	235 ± 36	–	ND	
213641358+572204113	876 ± 41	589 ± 53	272 ± 178	–	–	ND	
213642470+572523186	1513 ± 56	1220 ± 55	1093 ± 201	1046 ± 86	1525 ± 100	Full	
213648190+573402084	1203 ± 32	686 ± 42	314 ± 155	1809 ± 67	–	ND	
213653210+572052112	732 ± 50	395 ± 52	673 ± 208	–	–	ND:	24 μ m marginal
213655201+573030103	38 820 ± 158	41 537 ± 165	41 378 ± 345	–	43 405 ± 11034	Class I	
213655283+572551668	3304 ± 56	1803 ± 43	1195 ± 252	1045 ± 53	2166 ± 101	TD	
213658737+573848181	2764 ± 60	2294 ± 54	2463 ± 205	1866 ± 86	16 507 ± 456	PTD	
213659108+573905636	6278 ± 62	6339 ± 53	7337 ± 209	10 397 ± 91	47 929 ± 108	Full	
213659472+573134908	5918 ± 18	5496 ± 50	5118 ± 213	8387 ± 48	–	Full	
213701319+573418289	1616 ± 53	1282 ± 54	1091 ± 210	887 ± 79	6561 ± 106	TD	
213701401+572445873	5219 ± 61	3358 ± 61	3050 ± 272	1278 ± 73	–	ND:	24 μ m marginal

Notes. The full table is available at the CDS. Under “SED” we specify the SED type (ND = no disk; Class I = Class I object; Full = typical full disk; TD = transition disk; PTD = pre-transition disk; Dep. = dust-depleted disk; Unc. = Uncertain SED type). Objects listed as “marginal detection” at 24 μ m have probably excesses but their photometry is compromised by low S/N or different sources of contamination.

Table A.4. WISE data for confirmed members and probable members.

Spect. ID	WISE-1 (mJy)	WISE-2 (mJy)	WISE-3 (mJy)	WISE-4 (mJy)
213633647+573517477	11.54 ± 0.26	5.85 ± 0.11	17.35 ± 0.15	3.56 ± 1.13 ^a
213639147+572953326	148.01 ± 3.54	164.49 ± 3.03	1699.31 ± 4.54	343.75 ± 12.03 ^a
213642470+572523186	1.63 ± 0.04	1.27 ± 0.03	8.44 ± 0.09	2.38 ± 0.99 ^a
213655283+572551668	3.68 ± 0.08	1.80 ± 0.04	5.26 ± 0.10	2.56: ^a
213659108+573905636	6.55 ± 0.15	6.66 ± 0.12	156.60 ± 0.30	54.89 ± 1.77 ^a
213701319+573418289	1.66 ± 0.06	1.25 ± 0.04	27.49 ± 0.13	10.13 ± 1.65 ^a
213708137+573616213	2.36 ± 0.06	2.14 ± 0.05	28.03 ± 0.19	9.78 ± 1.04 ^a
213708879+572107012	1.75 ± 0.04	1.41 ± 0.04	5.01 ± 0.10	2.06:
213716349+572640200	6.98 ± 0.15 ^a	7.69 ± 0.15 ^a	111.07 ± 0.23	46.63 ± 1.63
21372447+5731359	2.64 ± 0.07	2.48 ± 0.06	43.61 ± 0.15	7.93 ± 0.93 ^a
213726148+572330562	0.39 ± 0.01	0.28 ± 0.01	10.82 ± 0.10	3.12: ^a
213732341+572503204	4.03 ± 0.09	3.44 ± 0.07	50.07 ± 0.17	18.94 ± 1.06 ^a
213734649+571657705	2.33 ± 0.06	2.06 ± 0.05	22.18 ± 0.14	11.55 ± 0.77 ^a
213738830+572936901	13.20 ± 0.29	12.68 ± 0.24	143.22 ± 0.33	30.64 ± 1.21
213740471+573433203	1.66 ± 0.04	1.72 ± 0.03	72.11 ± 0.23	48.74 ± 1.80
213742167+573431486	0.86 ± 0.02 ^a	0.82 ± 0.02 ^a	9.69 ± 0.12	9.14 ± 0.96 ^a
213742758+573325074	59.06 ± 1.14 ^a	61.98 ± 1.03 ^a	857.42 ± 1.03	155.84 ± 3.59 ^a
21374388+5734521	1.00 ± 0.04	0.96 ± 0.03	3.20 ± 0.13	3.93 ± 1.06 ^a
213744543+572200213	0.44 ± 0.02	0.41 ± 0.02	3.40 ± 0.15	2.20 ± 0.65
213746871+573156208	1.80 ± 0.05	1.66 ± 0.04	19.09 ± 0.17	11.19 ± 1.01 ^a
213747963+573242323	3.98 ± 0.10	3.22 ± 0.07	56.75 ± 0.24	24.11 ± 1.40 ^a
213751210+572436151	1.28 ± 0.03	1.24 ± 0.03	16.08 ± 0.16	7.45 ± 0.71 ^a
213756779+573448171	0.69 ± 0.02	0.51 ± 0.02	2.67: ^a	3.28 ^a
213809997+572352782	2.13 ± 0.05	2.13 ± 0.05	27.75 ± 0.16	2.52 ± 0.77
213812023+572500774	2.09 ± 0.05 ^a	1.52 ± 0.04 ^a	19.68 ± 0.13	3.97 ± 0.87
213812641+572033696	2.49 ± 0.06 ^a	2.03 ± 0.05 ^a	37.05 ± 0.18	8.97 ± 0.72

Notes. The full table is available at the CDS. Only good quality data in agreement with the *Spitzer* fluxes are taken into account (see text). Uncertain data are marked with “:”. Data that were not used in the SEDs (due to uncertainty or evident contamination) are marked with ^(a).

Table A.5. Other emission lines observed.

Spect. ID	Line λ (Å)	Obs. λ (Å)	EW (Å)
213659108+573905636	H α 6562.6	6562.5	-76.5
"	H β 4861.3	4860.9	-22.0
"	H δ 4101.7	4101.6	-7.2
"	H γ 4340.5	4340.1	-10.8
"	Ca II 8498.0	8498.2	-4.0
"	Ca II 8542.1	8542.1	-3.7
"	Ca II 8662.1	8662.2	-3.7
213659472+573134908	H α 6562.6	6564.5	-108.3
"	O I 8446.4	8446.0	-4.8
"	Ca II 8498.0	8497.9	-16.8
"	Ca II 8542.1	8541.9	-17.3
"	H I 8598.4	8598.2	-2.0
"	Ca II 8662.1	8662.0	-14.4
"	H I Pa 12 8750.5	8750.3	-1.7
"	H I Pa 11 8862.8	8862.8	-1.7
"	He I 5875.6	5875.6	-2.2
"	He I 6678.2	6677.6	-0.9
"	H β 4861.3	4862.3	-7.5
"	He I 4921.9	4923.9	-1.9
"	Fe II 5018.4	5018.3	-1.6
"	Fe II 5169.0	5168.6	-2.2
"	Ca II H 3933.7	3933.8	-4.3
"	Ca II K 3968.5	3968.0	-2.3
"	H γ 4340.5	4341.7	-1.8

Notes. The full table is available at the CDS. Stars with multiple emission lines and their identifications. The lines have been identified according to Sicilia-Aguilar et al. (2012), the NIST database, Appenzeller et al. (1986), and Hamman & Persson (1992). ^(a) Probably nebular.

Appendix B: SEDs of all the members with IR excesses

The following figures show the SEDs of all the members with IR excesses. Only those with clear excess are displayed; objects with uncertain colors (for instance, due to nebular contamination or contamination by a nearby object) are not displayed, but marked in Table A.3. Objects without an evident IR excess are also not displayed, since they are consistent with bare photospheres. According to the definitions in the main text, the SEDs have been organized by disk types:

- Typical full-disks, with strong IR excesses and evidence of ongoing accretion (see Figs. B.1 and B.2).
- Transition disks, candidates to have inner holes or inside-out evolution, with $[3.6]-[4.5] < 0.2$ and strong excesses at $24 \mu\text{m}$ (Fig. B.3).
- Pre-transitional disks, candidates to inner gaps (Espaillat et al. 2010), with reduced near-IR excesses, and strong $8 \mu\text{m}$ (and $24 \mu\text{m}$) fluxes (Fig. B.4).
- Dust-depleted disks, candidates to low small-dust mass given their reduced IR excesses at all wavelengths, specially at $24 \mu\text{m}$. Note that some of the transition disks have also very low excesses, so they are also candidates for dust depletion (or candidates for homologously depleted disks; Fig. B.5).
- Class I objects, consistent with very embedded objects with strong accretion and remnant envelopes (all associated to dense parts in the IC 1396A nebula; Fig. B.6).
- Finally, a few objects (usually with very small excesses, uncertain photometry, and/or likely contamination by nearby bright sources; see Fig. B.6) cannot be safely classified in any of the previous groups; they are therefore labeled and excluded from most plots and statistical analysis.

Probable members are labeled as “P”, all other SEDs correspond to confirmed members. In addition, information on the spectral type and the $H\alpha$ emission is also given in the plot, and the data are compared to a MARCS model with the appropriate spectral type (Gustafsson et al. 2008).

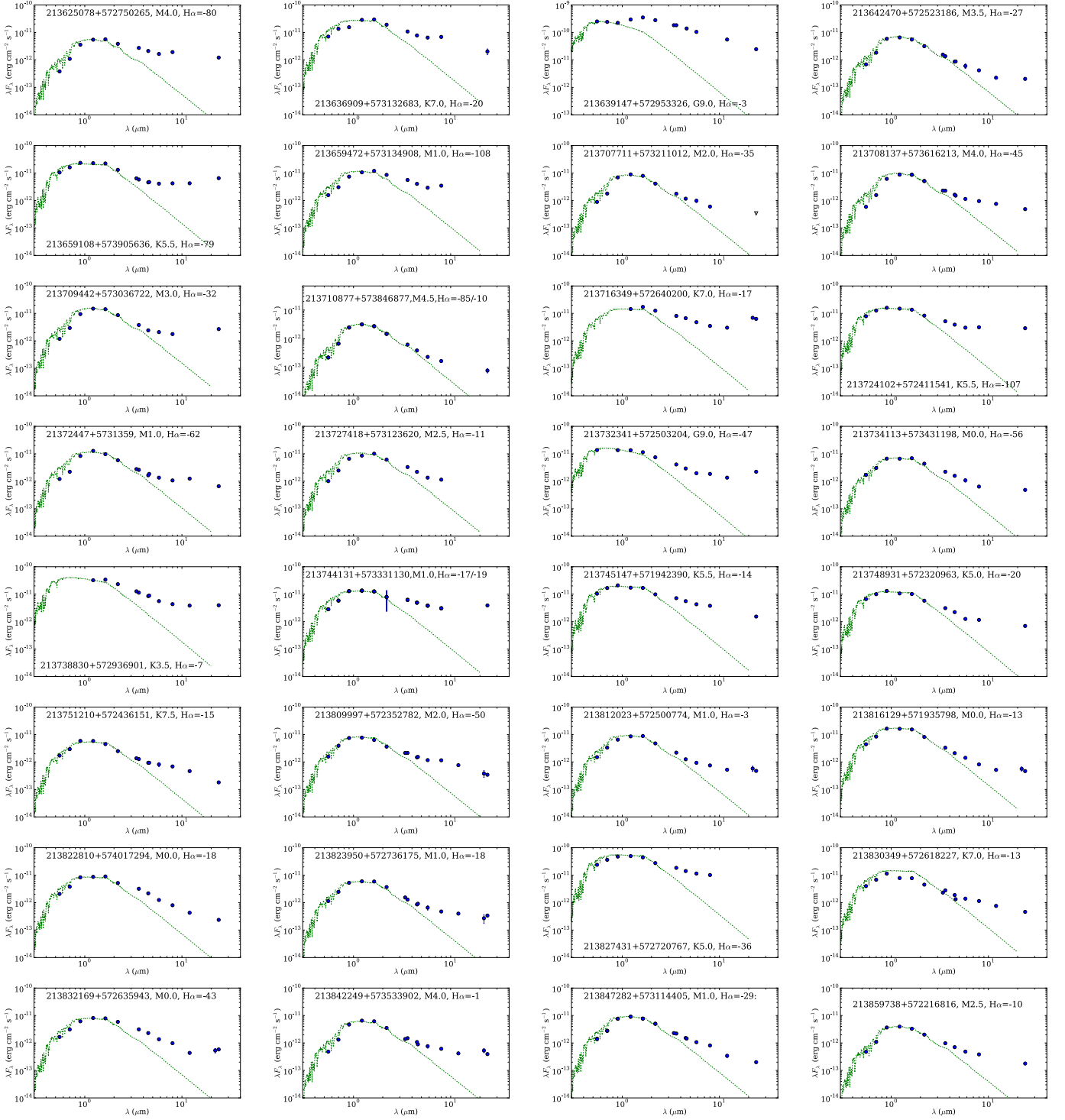


Fig. B.1. SEDs of the members and probably members with IR excess typical of full-disks. Inverted triangles represent upper limits.

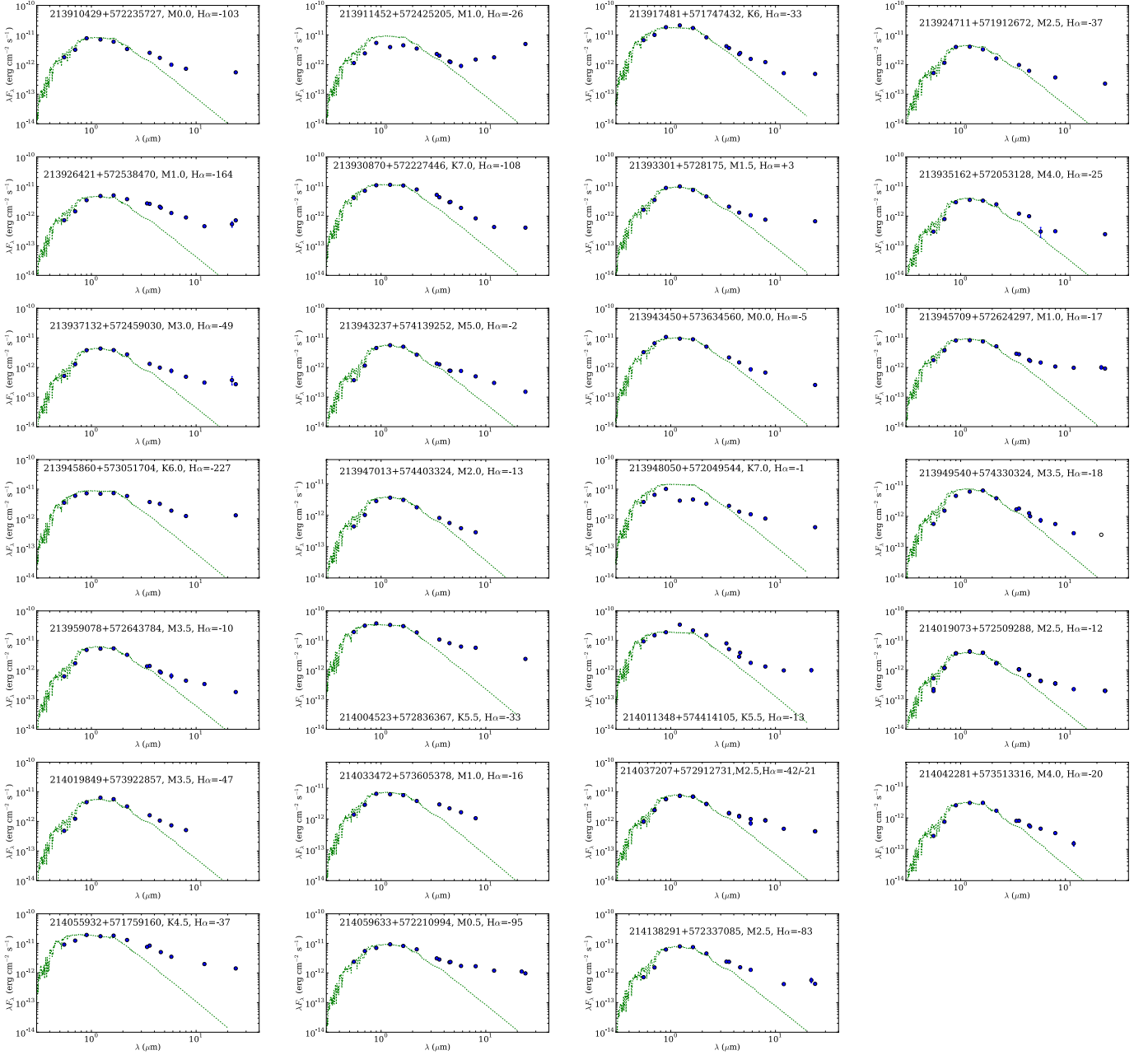


Fig. B.2. SEDs of the members and probably members with IR excess typical of full-disks (continued). 213917481+571747432 has strong $8 \mu\text{m}$, could be PTD. 213911452+572425205 has $[3.6]-[4.5] = 0.27$ and a strong kink in the SED, it could be a PTD although its $24 \mu\text{m}$ flux is likely contaminated by cloud emission. 214011348+574414105 has $[3.6]-[4.5] = 0.11$ but a SED that suggests strong variability and a flared, massive full-disk.

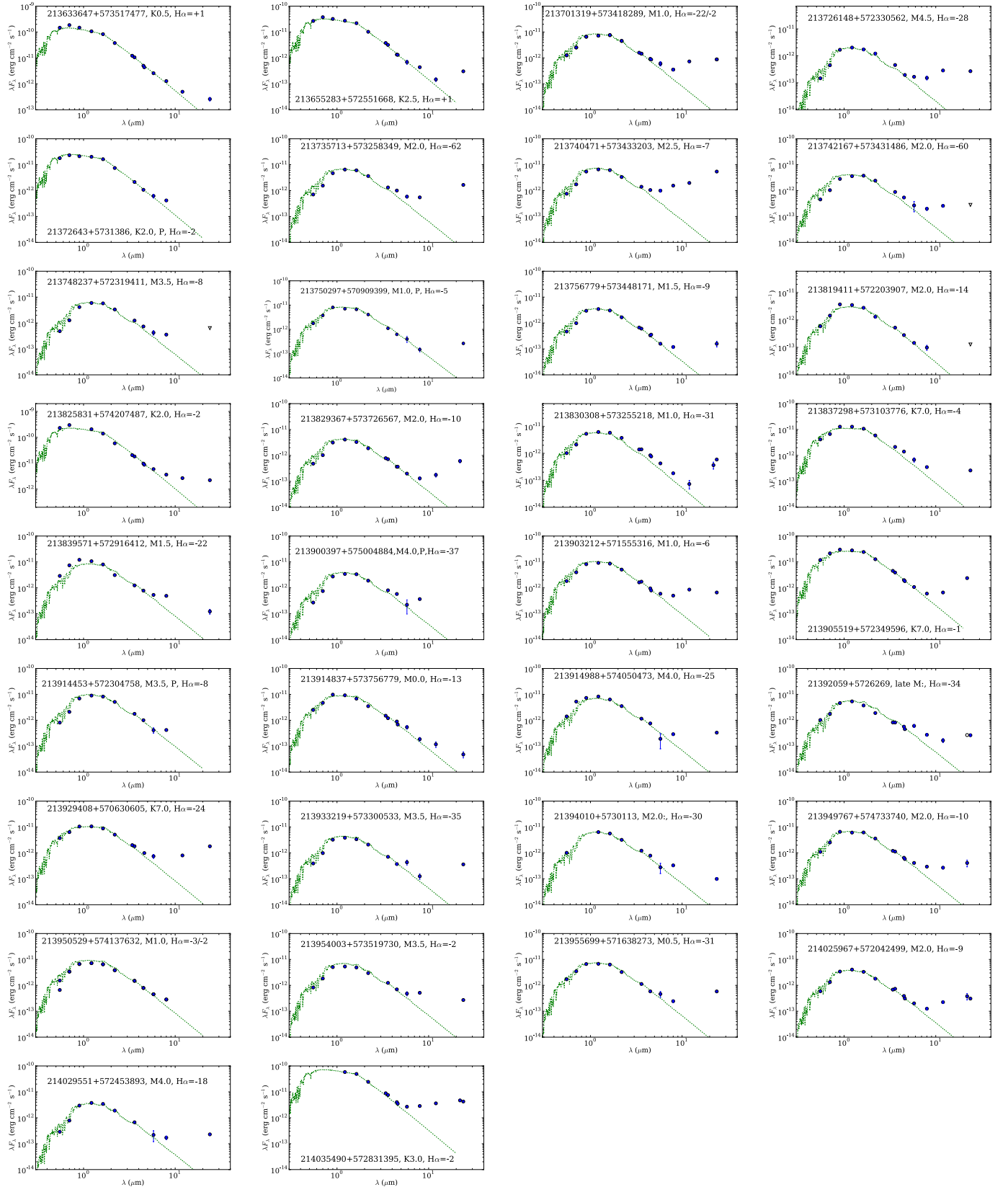


Fig. B.3. SEDs of the members and probably members with IR excess consistent with TD. Objects like 213819411+572203907, 213839571+572916412, 21394010+5730113 may be also dust-depleted. 213750297+570909399 may be partially contaminated by nebular emission but the detection is real. Inverted triangles mark upper limits, and open circles are uncertain values.

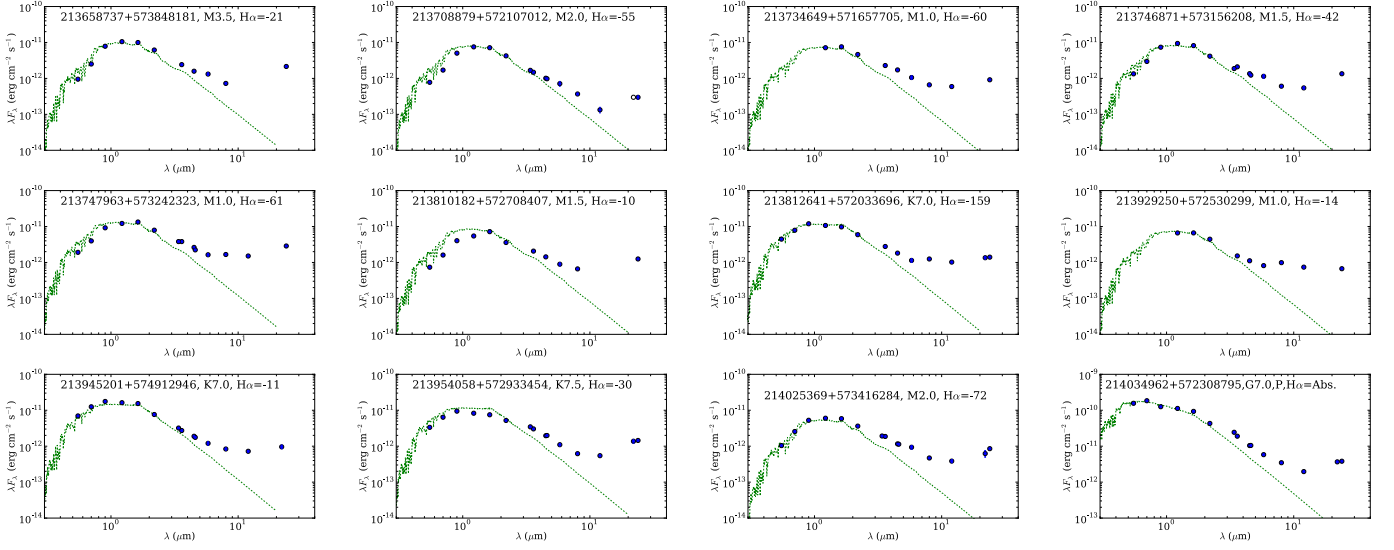


Fig. B.4. SEDs of the members and probably members with IR excess consistent with PTD. Note that the $24\ \mu\text{m}$ flux of 213810182+572708407 is contaminated by a nearby star, but the object still presents the kink in the SED typical of PTD.

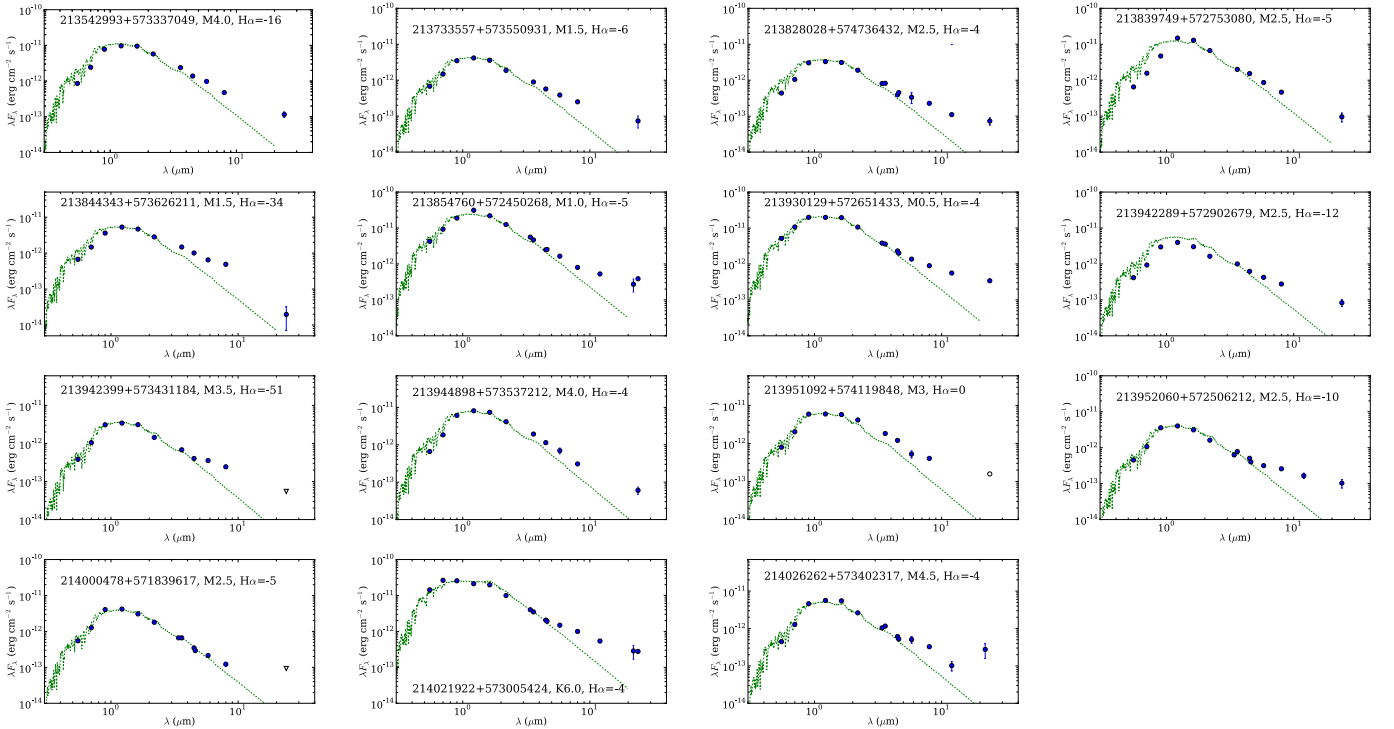


Fig. B.5. SEDs of the members and probably members with low IR excess consistent with dust-depleted disks. This includes objects with disks but no significant $24\ \mu\text{m}$ detection, in cloud-free regions. Some objects like 213844343+573626211 could be truncated disks. Objects like 213839749+572753080, 213854760+572450268, 213944898+573537212, 214000478+571839617, 214021922+573005424, and 214026262+573402317 may also have inner holes being thus both transitional and dust-depleted disk candidates. Inverted triangles mark upper limits, and open circles are uncertain values.

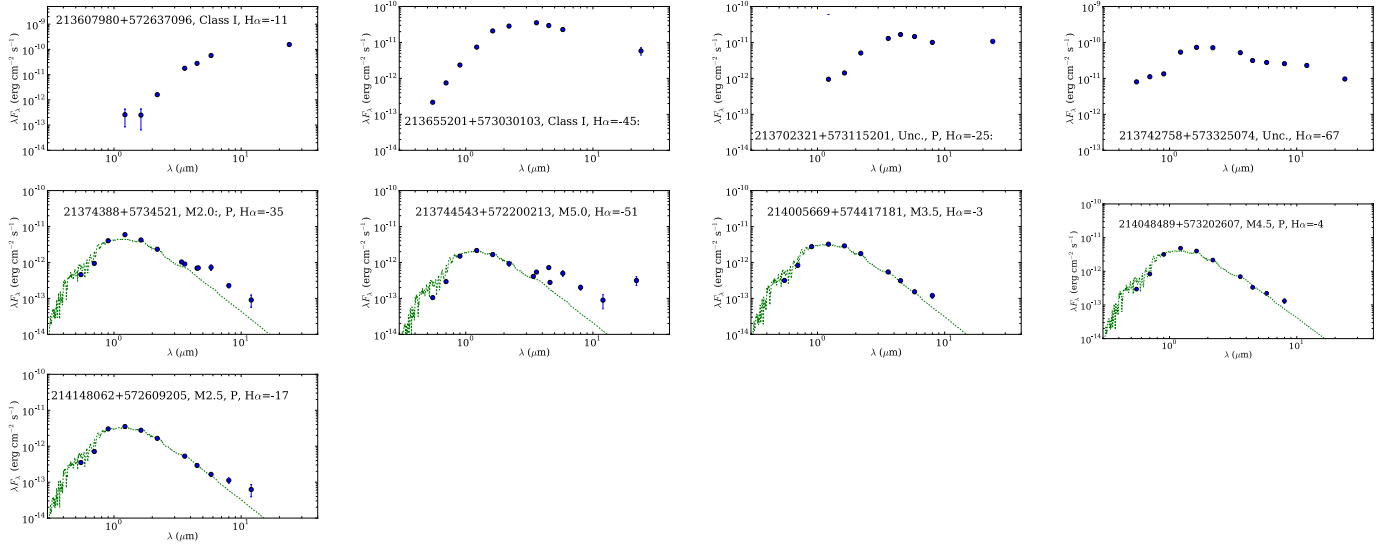


Fig. B.6. SEDs of the members and probably members with IR excess typical of Class I objects, early-type very embedded stars, and uncertain objects within the cloud. 21374388+5734521 is an uncertain case that could be a depleted disk or a combination of two sources. In the case of 214005669+574417181, 214048489+573202607, and 214148062+572609205, the small excess at $8\ \mu\text{m}$ with uncertain photometry does not allow us to determine if they are TD or diskless sources. These sources are not included in the statistics of disk types discussed in the text.